

PHOTOACOUSTIC AND RELATED PHOTOTHERMAL TECHNIQUES

H. VARGAS

Instituto de Física, Universidade Estadual de Campinas, 13100 Campinas, SP, Brazil

and

L.C.M. MIRANDA

*Laboratório Associado de Sensores e Materiais, Instituto de Pesquisas Espaciais,
12201 São José dos Campos, SP, Brazil*



NORTH-HOLLAND - AMSTERDAM

PHOTOACOUSTIC AND RELATED PHOTOTHERMAL TECHNIQUES

H. VARGAS

Instituto de Física, Universidade Estadual de Campinas, 13100 Campinas, SP, Brazil

and

L.C.M. MIRANDA

Laboratório Associado de Sensores e Materiais, Instituto de Pesquisas Espaciais, 12201 São José dos Campos, SP, Brazil

Received July 1987

Contents:

1. Introduction	45	5. Infrared photoacoustic spectroscopy	72
2. Photoacoustic principles and detection techniques	45	6. Thermal diffusivity measurements	75
2.1. PA signal generation – Standard model	46	7. Investigation of phase transitions	80
2.2. Extended models	48	8. Deexcitation processes	84
2.3. Detection techniques	52	9. Biological applications	92
3. Depth-profile analysis and microscopy	62	10. Concluding remarks	96
4. Microwave spectroscopy	67	References	96

Abstract:

We review the theory and applications of the photoacoustic and related methods belonging to the general area of photothermal measurement techniques. This essay is intended for researchers especially unfamiliar with the basic ideas and potentialities of this rapidly developing field. The applications of photothermal techniques include spectroscopic applications, such as infrared and microwave spectroscopies, monitoring of non-radiative deexcitation processes, biological applications, and measurements of thermal properties.

Single orders for this issue

PHYSICS REPORTS (Review Section of Physics Letters) 161, No. 2 (1988) 43–101.

Copies of this issue may be obtained at the price given below. All orders should be sent directly to the Publisher. Orders must be accompanied by check.

Single issue price Dfl. 45.00, postage included.

1. Introduction

A very active area of research in applied physics these days comes under the general heading of photoacoustic (PA) or photothermal phenomena. These terms are meant to imply the generation of acoustic waves or other thermoelastic effects by any type of incident energetic beam ranging from electromagnetic radiation from radio to X-ray, electrons, protons, ultrasound, etc. The PA effect was discovered by A.G. Bell in 1890 and the modern revival of this field was experimentally and theoretically pioneered by the works of Kreuzer [1] and Rosencwaig [2–4] in the early seventies. Nowadays, photoacoustics has expanded to encompass several other, not exclusively acoustic, thermal detection techniques and has been successfully applied to several problems in physics, chemistry, biology, medicine and engineering. Apart from its versatility in the detection systems with varying degree of sensitivity, as well as its capability for depth profile analysis, the photoacoustic and related photothermal techniques are bound to become an important approach for nondestructive testing. This is reflected by the increasing interest in the application of these techniques to nondestructive testing at the latest International Meeting of Photoacoustic, Thermal and Related Sciences held at Montreal. From what has been presented at this Meeting, industrial applications of the photothermal techniques do not seem to be far away.

A glance at the table of contents reveals that this review focuses on a modest collection of applications that have been reported in the literature. The photoacoustic literature is expanding so rapidly that no review at this time is likely to be complete. The subjects reviewed in this paper reflect our own interest in the field and so we apologize in advance to the many authors whose work we have not cited. For a complementary reading, the interested reader may refer to the other reviews given by Rosencwaig [5], Patel and Tam [6], Kinney and Staley [7], Kirkbright and Castleden [8], West et al. [9], Klein et al. [10], as well as to the books of Pao [11], Rosencwaig [12], and Mandelis [13].

A general overview of the photoacoustic principles and detection techniques is given in the following section. In sections 3 to 9, several applications of these techniques are discussed. These include the PA microscopy, photothermal characterization, non-radiative process studies, and biological spectroscopic applications.

2. Photoacoustic principles and detection techniques

The underlying principle of photoacoustics is the heating produced in a sample due to the absorption of an incident energetic beam. The absorption of an incident energetic beam and the subsequent non-radiative deexcitation–relaxation processes give rise to a heat source in the sample, which may be distributed throughout its volume or confined to its surface. This heat source gives rise to both temperature and pressure fluctuations within the samples, which are then detected by thermal or acoustic, or even both, sensing devices. In most cases, the heat deposited in the sample is due to the absorption of optical radiation and this is the reason for the name photoacoustic and photothermal associated with these techniques.

Physically, the heating of the sample by the incident beam depends not only on the amount of heat generated in the sample, i.e. on the sample absorption coefficient for the incident radiation as well as the light-into-heat conversion efficiency, but also on how this heat diffuses through the sample. It is therefore intuitively sound to expect that the detected PA signal should be strongly dependent upon the interplay of these three factors. The dependence upon these factors is the main reason underlying the

versatility of the PA technique. The dependence of the PA signal on the absorption coefficient for the incident radiation allows us to perform spectroscopic studies, whereas the fact that the signal is also proportional to the light-into-heat conversion efficiency means that it is complementary to other photoinduced energy conversion processes. In this way, the PA technique can also be used for getting information concerning the non-thermal deexcitation processes.

Finally, the fact that the PA signal depends on how the heat diffuses through the sample allows us to perform not only thermal characterization of the sample (i.e. measurements of its thermal properties, like thermal diffusivity and thermal conductivity) but also to conduct thermal imaging. This last point comes from the fact that the thermal wave generated by the absorption of an incident energetic pulse may be reflected and scattered as it encounters cracks, defects, and so on, thereby affecting the detected signal. In what follows we review the quantitative analysis of the PA signal as well as the various detection techniques.

2.1. PA signal generation – Standard model

The standard model describing quantitatively the PA signal of a solid sample was proposed by Rosenzweig and Gersho [14, 15]. These authors, based upon an earlier suggestion by Parker [16], showed that the periodic heat flow between the sample and the gas of the closed cell is the basic mechanism responsible for the acoustic signal. The standard photoacoustic cell configuration is systematically shown in fig. 1. It consists of a solid sample in a small, gas-filled cell, at a distance l_g from a transparent window through which a modulated radiation beam is incident. A condenser microphone is mounted in one of the lateral cell walls to detect the acoustic signal produced in the gas chamber. According to the Rosenzweig and Gersho model (RG model) [15] the pressure fluctuation is solely determined by the temperature distribution in the sample–gas–backing system of fig. 1. Assuming sinusoidally modulated light, at a frequency $\omega = 2\pi f$, with intensity

$$I = \frac{1}{2} I_0 (1 + e^{j\omega t}), \quad (1)$$

incident on the sample, and denoting by β and η the sample optical absorption coefficient and the light-into-heat conversion efficiency, respectively, RG have solved the thermal diffusion equation of the three-media system of fig. 1. The result they got for the temperature fluctuation in the gas T_g can be written as [15]

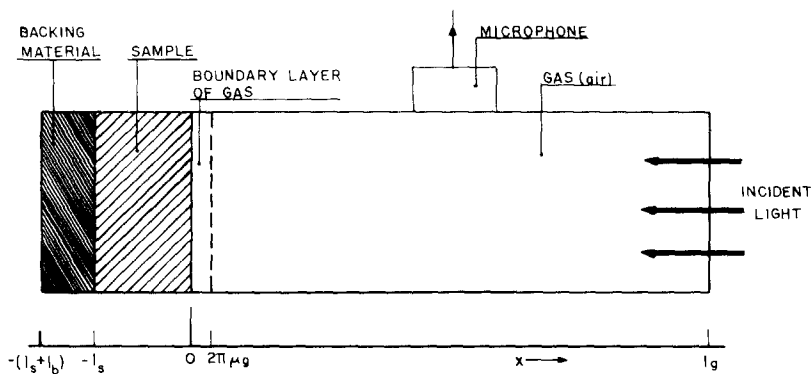


Fig. 1. Schematic photoacoustic cell configuration.

$$T_g = \theta e^{-\sigma_g x} e^{j\omega t}, \quad (2)$$

where

$$\theta = \frac{\beta I_0}{2k_s(\beta^2 - \sigma_s^2)} \frac{(r-1)(b+1)e^{l_s\sigma_s} - (r+1)(b-1)e^{-l_s\sigma_s} + 2(b-r)e^{-\beta l_s}}{(g+1)(b+1)e^{l_s\sigma_s} - (g-1)(b-1)e^{-l_s\sigma_s}}. \quad (3)$$

In eqs. (2) and (3) $\sigma_i = (1+j)a_i$, $a_i = (\omega/2\alpha_i)^{1/2}$, $r = \beta/\sigma_s$, $b = k_b\sigma_b/k_s\sigma_s$, $g = k_g\sigma_g/k_s\sigma_s$. Here the index i denotes the backing ($i=b$), sample ($i=s$), and gas ($i=g$) media, and k_i is the thermal conductivity, ρ_i the density, c_i the specific heat, and $\alpha_i = k_i/\rho_i c_i$ the thermal diffusivity of medium i . As can be seen from eq. (2), the temperature fluctuation in the gas attenuates rapidly to zero with increasing distance from the surface such that, at a distance $2\pi\mu_g$, where $\mu_g = a_g^{-1}$ is the thermal diffusion length in the gas, the temperature fluctuation is effectively fully damped out. RG then argue that only a gas boundary layer of thickness $2\pi\mu_g$ close to the sample surface is capable of responding thermally to the periodic temperature fluctuation at the sample surface, thereby acting as an acoustic piston to the rest of the gas column. Assuming that this gas column responds to the action of this piston adiabatically, the acoustic pressure in the cell is calculated from the adiabatic gas law as

$$\delta P = \frac{\gamma P_0 \theta}{l_g \sigma_g T_0} e^{j\omega t}. \quad (4)$$

Even though the above expression for the PA signal is quite complicated, there are some important limiting cases where it is simple to analyse. These cases are grouped according to the optical and thermal opaqueness of the sample. An optical thin (thick) sample corresponds to the case where $\beta l_s \ll 1$ ($\gg 1$), whereas a thermally thin (thick) sample corresponds to the case where $l_s a_s \ll 1$ ($\gg 1$). For example, it is shown by RG [15] that for an optically transparent sample the pressure fluctuation δP is always proportional to the optical absorption coefficient. This implies that one can perform spectroscopic studies by measuring the acoustic signal in the gas chamber. Furthermore, a detailed analysis of eq. (4) shows that the amplitude of the PA signal also exhibits a marked modulation frequency dependence in such a way that the signal decreases with increasing modulation frequency. These two facts together point at a unique capability of photoacoustic spectroscopy, namely to obtain a depth profile of optical absorption within the sample. That is, by starting at a high modulation frequency, the thermal diffusion length in the sample, $\mu_s = (\alpha_s/\pi f)^{1/2}$, is small so that the surface heating of the sample is basically due to the optical absorption by a layer of material near the sample surface. Then, by decreasing the modulation frequency, we increase the thermal diffusion length and obtain optical absorption data deep into the sample. This depth-profile analysis capability is unique to photothermal techniques and has opened up a wide range of applications for photoacoustic spectroscopy. In table 1 we summarize the dependence of the PA signal on the optical and thermal parameters of the sample as well as its modulation frequency dependence as predicted by the RG model. Here we note that the spectra of highly opaque samples can now be measured by PA spectroscopy.

The above theory for the PA signal was extensively tested both with solid and liquid samples in a wide range of modulation frequencies and power intensities. For example, the modulation frequency dependence of the PA signal predicted by the RG model was verified by Adams et al. [17] using thin polymer films as well as by Rosenzweig [18] for the case of a GaP sample and by Wetsel and McDonald [19] for an aqueous phenol red sodium salt solution. The saturation of the PA signal expected to occur

Table 1
Dependence of the PA signal amplitude on the optical and thermal properties as predicted by the RG model in some limiting cases.

Case	Approximate PA signal amplitude
$\beta l_s \ll 1, l_s \ll \mu_s$	$\beta l (\alpha_g \alpha_t)^{1/2} / k_g f$
$\beta l_s \ll 1, l_s \ll \mu_s$	$\beta \alpha_g \alpha_t^{1/2} / k_g f^{3/2}$
$\beta l_s \gg 1, l_s \ll \mu_s, \beta \mu_s \gg 1$	$(\alpha_g \alpha_t)^{1/2} / k_g f$
$\beta l_s \gg 1, l_s > \mu_s, \beta \mu_s > 1$	$(\alpha_g \alpha_t)^{1/2} / k_g f$
$\beta l_s \gg 1, l_s \gg \mu_s, \beta \mu_s < 1$	$\beta (\alpha_g \alpha_t)^{1/2} / k_g f^{3/2}$

in an optically opaque sample when the thermal diffusion length becomes larger than the optical penetration depth (cf. table 1) has been investigated by McClelland and Kniseley [20] using a variable β sample by working with aqueous solutions of methylene blue dye. The possibility of getting absolute measurements of the optical absorption coefficient using PA spectroscopy was checked by Wetsel and McDonald [19], by Cesar et al. [21] for the case of MnO_2 -impregnated polyethylene and by several other authors [22–24]. Finally, the range for the absorption coefficient β that can be measured by PA spectroscopy was investigated by several authors. For powdered amorphous As_2S_3 [25] β greater than 10^5 cm^{-1} was measured at a modulation frequency of 5 kHz. At the lower end, absorption coefficients as low as 10^{-5} cm^{-1} have been measured in alkali fluoride crystals by Hordvik and Schlossberg [26] using piezoelectric detection.

2.2. Extended models

Following the success of the thermal piston model of RG described above, several authors [27, 29–33] have considered different effects improving the understanding of the PA signal generation. The RG theory is based upon two central assumptions, namely, that the gas chamber length l_g is much larger than the gas thermal diffusion length, i.e. $l_g a_g \gg 1$, and much smaller than the acoustic wavelength $\lambda_s = v_s / f$, where v_s is the sound velocity in gas. In refs. [27] and [29–31] it is pointed out that this is a weak aspect of the RG model in the sense that it cannot account for the roll-off in the PA signal amplitude when the gas column is thermally thin or when l_g approaches a considerable fraction of the acoustic wavelength. In particular, McDonald and Wetsel [29] have proposed that a more adequate description of the PA signal should be based on the solution of the coupled thermoelastic equations for temperature and pressure, namely,

$$-k\nabla^2 T + \rho c_p \frac{\partial T}{\partial t} = S + \frac{\rho c_p}{B\beta_T} \frac{\gamma - 1}{\gamma} \frac{\partial p}{\partial t}, \quad (5)$$

$$B\nabla^2 p - \rho \frac{\partial^2 p}{\partial t^2} = -\rho B\beta_T \frac{\partial T}{\partial t}, \quad (6)$$

where c_p is the specific heat at constant pressure, γ is the specific heat ratio, B is the bulk modulus, β_T is the volume thermal expansion coefficient, and S is heat source resulting from the radiation beam absorption. This coupled set of equations for the temperature and pressure is then applied to the three regions (backing–sample–gas) of the photoacoustic cell. In the case of solids, $\gamma \approx 1$, so that the acoustic

term in eq. (5) has negligible effect on the temperature equation. The temperature distribution in the sample is therefore readily obtained from the thermal diffusion equation solution, which then acts as the source term for the pressure equation. The main effect of taking into account the acoustic coupling in the description of the PA signal is that the thermally induced expansion and contraction of the sample surface also contributes to the PA signal. This is the basis of the “composite piston” model, of McDonald and Wetsel [29], in which the thermal piston effect of RG and the sample vibration effect both contribute to the PA signal. However, this surface vibration effect is frequently small compared to the thermal piston effect, except in the case of weak absorption (transparency) at high modulation frequencies.

In fig. 2 we reproduce the theoretical dependence of the PA signal for an aqueous dye as given by McDonald and Wetsel [29]. The solid lines correspond to the results from the composite piston model whereas the dashed lines are the results of the RG thermal piston model. It is clear from fig. 2 that, as the absorption coefficient decreases, the effect of sample vibration becomes important, especially at high modulation frequencies. McDonald and Wetsel have not only verified this prediction experimentally, on aqueous solutions of phenol red sodium salts, but could also explain the roll-off of the PA signal at small gas column length. For a more recent discussion on the composite piston model we refer to ref. [34].

The RG, the composite piston [29], and the Aamodt et al. [27] models have recently been criticized by Korpiun and collaborators [35–37]. Korpiun and Büchner [35] were interested in explaining the PA effect down to arbitrarily low frequencies and small gas length, $l_g a_g \ll 1$. In the course of their work they noted that two important points have been overlooked by several authors. First, for a thermally thin gas, the influence of the residual volume (i.e. the volume that is left over when the gas length approaches zero) on the PA signal should be taken into account. This residual volume consists of the

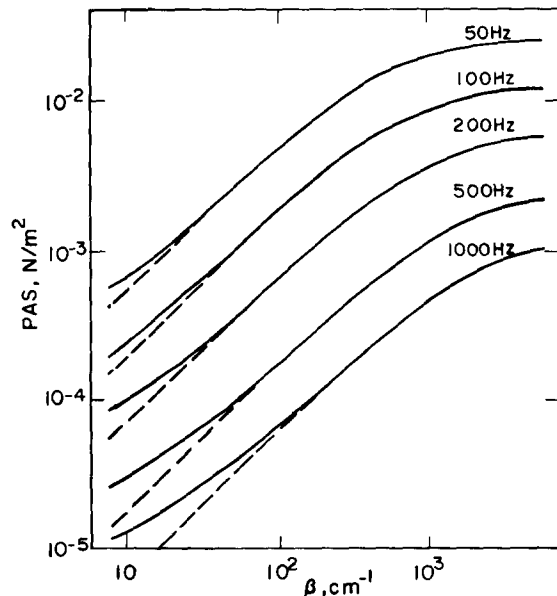


Fig. 2. Theoretical dependence of the PA signal amplitude on the optical absorption coefficient for an aqueous dye solution. The solid lines correspond to the results from the composite piston model while the dashed lines are the results from the RG model (after McDonald and Wetsel [29]).

volume occupied by the gas in front of the microphone diaphragm and that of the channel connecting it with the active volume of the cell chamber. This is schematically shown in fig. 3. The second, and more fundamental, point raised by Korpiun and Büchner [35] regards the assumption, implicit in the RG model, that the pressure fluctuation in the gas chamber is described as an isobaric–adiabatic process. These authors argued that the temperature–pressure relationship should be described by an isochoric (constant volume) rather than by an isobaric–adiabatic process. This description of PA signal generation may be summarized as follows. Consider the cylindrically shaped PA configuration shown in fig. 3. The cross section A_c of the gas chamber is $A_c = \pi R_c^2$ and the cross section of the illuminated region of the sample is $A_s = \pi R_s^2$. The total volume V of gas in the PA cell consists of the active volume V_c and the residual volume V_r mentioned above, i.e.,

$$V = V_c + V_r .$$

Under the usual experimental conditions of modulation frequencies smaller than a few kHz, both the gas length l_g and cell diameter are much smaller than the sound wavelength (for 1 kHz the sound wavelength in air is of the order of 34 cm). The pressure fluctuation in the cell may then be considered constant in amplitude over the entire volume. The heat flow from the sample to the gas thus leads to a change in the internal energy U of the gas at constant volume. The relationship between the internal energy and pressure change for an isochoric process is

$$\delta U = \frac{\rho_g c_v V}{\beta_T B} \delta P , \quad (7)$$

where c_v is the specific heat at constant volume and the other parameters were defined previously. In terms of the average temperature fluctuation in the gas, $\delta T(t)$, the mean change of the gas internal energy is

$$\delta U = \rho_g c_v V_s \delta T(t) , \quad (8)$$

where

$$\delta T(t) = \frac{1}{l_g} \int_0^{l_g} dx T_g(x, t) , \quad (9)$$

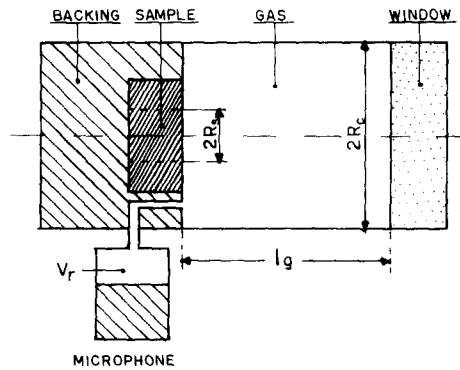


Fig. 3. Schematic PA cell showing the effective residual volume V_r .

and $V_s = A_s l_g$ is the volume of the gas column with cross section equal to the heated sample region, A_s , and length l_g . In eq. (9), $T_g(x, t)$ is the full solution to the thermal diffusion equation in the gas, as described previously in the RG model, including, however, the entrance window. Combining eqs. (7), (8) and (9), and remembering that for an ideal gas $\beta_T = T_0^{-1}$ and $B = P_0$, where T_0 (P_0) is the ambient temperature (pressure), one gets

$$\delta P(t) = \frac{P_0}{T_0} \delta T(t). \quad (10)$$

Calculations of (10) as a function of l_g have been carried out by Korpiun and Büchner [35], who showed that for $l_g \rightarrow 0$, the pressure fluctuation vanishes. As one increases l_g , the signal goes through a maximum when l_g is approximately equal to the thermal diffusion length a_g^{-1} , and on further increasing l_g , it then decreases as l_g^{-1} , as in RG model. In the limit of a thermally thin gas ($l_g a_g \ll 1$)

$$|\delta P| \approx \frac{I_0 P_0 \beta K' R_s^2}{2\sqrt{2} T_0 R_c^2 [1 + (V_r/A_c l_g)]}, \quad (11)$$

where K' is a complicated expression depending upon the sample and backing physical parameters, and is independent of the thermal properties of the gas. As l_g approaches zero, the amplitude of the pressure fluctuation given by eq. (11) becomes proportional to the gas column length l_g and is the same for all gases. This point is an important result, which was readily verified experimentally by Korpiun and Büchner [35]. In contrast, for a thermally thick gas ($l_g a_g \gg 1$), the extended model of ref. [35] predicts that

$$|\delta P| \approx \frac{I_0 P_0 \beta K'' R_s^2}{2\sqrt{2} T_0 R_c^2 l_g a_g [1 + (V_r/A_c l_g)]}, \quad (12)$$

where, again, K'' is a given function of the sample and backing physical parameters. For $V_r \ll A_c l_g$, eq. (12) reduces to the RG result given by eqs. (3) and (4) except for the presence of the multiplying factor $\gamma = c_p/c_v$ in front of it. I.e., the RG model predicts that, for a thermally thick gas $|\delta P| \sim \gamma/l_g a_g$, whereas the Korpiun and Büchner model predicts that $|\delta P| \sim 1/l_g a_g$, as $l_g a_g \gg 1$. In fig. 4 we show the theoretically predicted behavior of the pressure fluctuation from graphite as a function of the gas length for a cell filled with He, N₂, and freon 13 at a modulation frequency of 100 Hz as given in ref. [35]. In table 2, we summarize the experimental results of Korpiun and Büchner [35] for the PA signal of a carbon-black using several filling gases. The comparison between the predictions of the RG model with the ones of ref. [35] for the ratio of the PA signal for the various gases relative to the one of the argon-filled cell clearly shows that the PA signal forming process is isochoric rather than adiabatic.

In subsequent papers Korpiun and collaborators [36, 37] have next investigated the influence of gas viscosity on the PA signal in gas-microphone cells. They have shown that the viscous damping in the cell significantly affects the PA signal at small gas length, especially at high modulation frequencies. Further aspects of the PA signal of solid samples have also been the subject of considerable attention by several authors. For example, the PA signal of samples with continuously varying optical and thermal properties have been dealt with in refs. [28, 38, 39].

The influence of the solid-gas and solid-solid thermal contact resistance was addressed by Cesar et al. [32] and later criticized in refs. [40–42]. In particular, it was shown by Parpal et al. [43] that in the

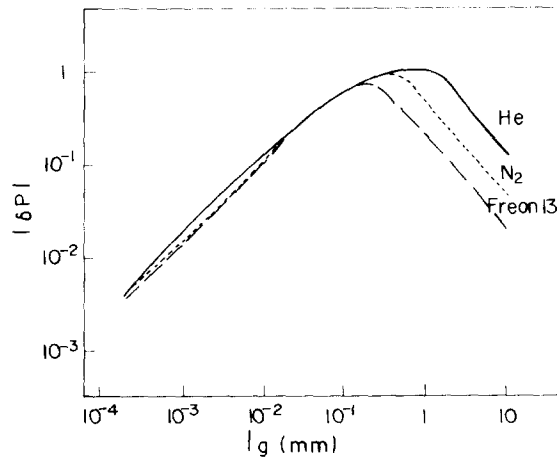


Fig. 4. Theoretical PA pressure amplitude for graphite as a function of the gas length for a cell filled with He, N₂, and freon 13 at a modulation frequency of 100 Hz (after Korpiun and Büchner [35]).

case of solid–solid contact the contribution of the thermal contact resistance should be taken into account. In the case of simply supported plate-shaped samples surrounded by air, the thermoelastic bending of the sample produces a significant contribution to the PA signal, especially in the case of thermally thick samples. This effect is essentially due to the temperature gradient set inside the sample along the incident radiation beam direction by the photothermal heating, and was originally discussed by Rousset et al. [44]. These authors have demonstrated the dominant role of this effect in the thermally thick region in both photothermal deflection and gas–microphone PA experiments using thin metallic disk-like samples. This effect was recently explored by Leite et al. [45] for measuring the thermal diffusivity of polymer foils, and by Torres-Filho et al. [46] for monitoring epoxy adhesive curing. A recent study by Perondi and Miranda [47] using a gas–microphone version of the so-called open photoacoustic cell, shows that the thermoelastic bending becomes increasingly important for samples with large thermal expansion coefficients such as polymer foils.

2.3. Detection techniques

So far we have emphasized the effects of just one mode through which the heat deposited in a sample is transferred to the surrounding media, namely heat conduction and diffusion. This is a non-cooperative and dissipative process in which the rate of energy transfer is determined by the

Table 2
PA signal from a carbon-black for several filling gases (after Korpiun and Büchner [35]).

Filling gases		$ \delta P_{A1} / \delta P_{gas} $		
		Isochoric model		
		Exp.	Theor.	RG model
$f = 9 \text{ Hz}, l_g = 0.5 \text{ mm}$	N ₂	0.94	1	1.19
	freon 13	0.95	1	1.48
$f = 150 \text{ Hz}, l_g = 4 \text{ mm}$	N ₂	0.99	0.97	1.15
	freon 13	2.23	2.22	3.16

thermal diffusivity $\alpha = k/\rho c$, and the distance of appreciable energy transfer is given by the thermal diffusion length μ , which for periodically deposited heat is $\mu = (2\alpha/\omega)^{1/2}$. The second mode by which the deposited heat can be transferred to the surrounding media is through a direct coupling to the vibrational modes (i.e. acoustic phonon spectrum) of the material, namely, via a thermoelastic process. The speed of energy transfer in this case is governed by the speed of sound in the material and the distance of appreciable energy transfer is essentially determined by the sample dimensions.

More generally, we may say that the photothermal heating of a sample leads to thermal and stress-induced changes in the physical properties of both the sample and the surrounding media. Based on this observation, several alternative detection techniques have been developed for monitoring the photothermally induced changes of given physical properties either of the sample or of its surrounding medium. The conventional gas–microphone PA detection technique described previously is just one example of this. It uses the enclosed gas in intimate contact with a sample in the PA cell as a transducer medium to detect the periodic heating of the sample. One can alternatively monitor several other physical properties of the sample such as the sample surface displacement or the changes in the refractive indices of both the sample and the surrounding medium to study the deposited heat. Each of these different techniques offers particular advantages for the specific applications envisaged. Some of the different contact-type detection techniques, such as the conventional PA microphone detection technique, or remote sensing techniques, which have been developed in the last ten years, are briefly reviewed in the remainder of this section.

2.3.1. Piezoelectric detection

This is a contact-type detection technique using a piezoelectric transducer (usually, a lead zirconate titanate (PZT) ceramic) attached directly to the sample. The absorption of the incident modulated light beam causes a temperature fluctuation of the illuminated volume. This leads to the expansion of that region, causing displacement of the sample surface by two separate mechanisms. First, there is the usual thermal expansion of both surfaces proportional to the spatially averaged temperature fluctuation of the sample. Second, the temperature decay along the sample thickness causes the front surface of the sample to expand more than the rear surface, thereby resulting in a bending of the sample, proportional to the average temperature gradient of the sample. The resulting expansion, caused by this thermoelastic bending mechanism, is then added to the normal thermal expansion, thereby producing a net displacement of the sample surface, which is sensed by the PZT as a voltage output between the two surfaces of the transducer.

The transducer can be assembled in different ways depending on the particular experiment. In figs. 5a and 5b we show two typical transducer assemblies for PZT detection in solid samples. One of them (fig. 5a) consists of attaching the PZT to the back surface of the sample, which is particularly good for the case of opaque samples. The other typical assembly consists of using a transducer in the form of an annulus located on either side of the sample. This is particularly useful for optically transparent samples. In the case of liquid samples the PZT transducer is mounted directly onto one of the walls of the liquid containing cell.

Piezoelectric detection has been used by several authors [48–52] for investigating both solid and liquid samples. Hordvik and Skolnik [49] have used it for measuring surface and bulk optical absorption of laser window materials, whereas Lahmann et al. [50], Oda et al. [51] and others have investigated the PA signal of liquids using PZT detection. Spectroscopic studies in powder and bulk samples using piezoelectric detection have also been carried out by Farrow et al. [52].

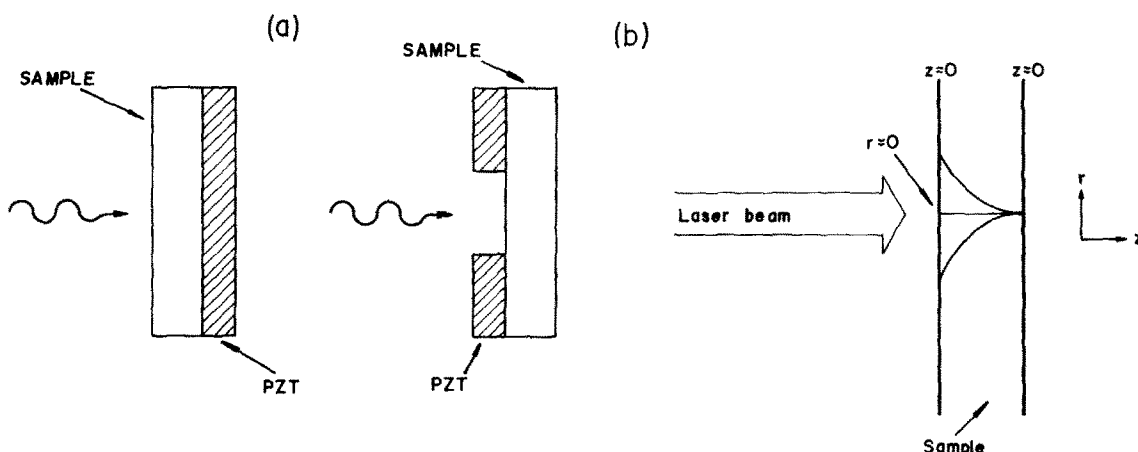


Fig. 5. Transducer assembly for PZT detection of solid opaque (a) and transparent (b) samples.

A slightly modified version of PZT detection, called open-photoacoustic cell, has been developed by Helander and collaborators [53–57]. It consists in measuring, with a PZT transducer, the expansion of a thin solid plate (usually a sapphire plate) in thermal contact with the sample. This technique has been successfully applied to study the optical spectra of liquids [53], sedimentation of whole blood [54], and to the discrimination of surface and bulk optical absorption [55]. The theory for this open-photoacoustic cell technique was described by Helander in refs. [56, 57].

A more compact version of Helander's open cell has been proposed by McQueen [58]. It consists of a sapphire disk mounted on a ring-shaped PZT crystal. The absorbing sample is placed on the sapphire window. When light is sent through the window and becomes partly absorbed by the sample, which is in thermal contact with the window, radial expansion gives rise to the electrical signal in the PZT. This open-cell sensor is shown in fig. 6. The wavelength of the incident light can either be swept in order to record an absorption spectrum, or kept fixed for specific quantitative analysis of a particular substance.

An equivalent open-cell sensor, using, however, a common miniature electret microphone instead of a PZT crystal, has recently been proposed by da Silva et al. [59], as an inexpensive infrared detector. In fig. 7 we show the open-cell sensor of da Silva et al. The radiation absorbing material (20 μm thick Al foil with a gold-black coating on the surface) is mounted directly onto a miniature commercial electret microphone. It uses the internal front air chamber adjacent to the metallized diaphragm as a conventional gas chamber of photoacoustics. Its advantages over conventional PA detectors are the use of a minimal gas chamber with no further transducer medium needed, no cell machining required, and low cost.

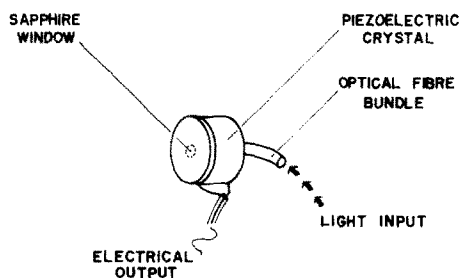


Fig. 6. Schematic ring-shaped open-cell sensor.

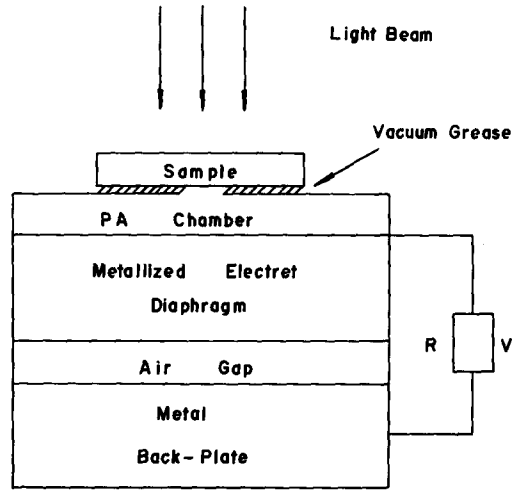


Fig. 7. Schematic open photoacoustic cell using the front air chamber of a common electret microphone as the transducer medium, as proposed in ref. [59].

Several aspects of the theory of the photothermal–piezoelectric signal have been discussed in refs. [52, 53, 60, 61]. For the typical PZT detection configuration of fig. 5, solving the coupled thermoelastic equations together with the continuity equation, the potential difference between the transducer electrodes can be written as [61]

$$V \simeq \frac{eL\alpha_T(1+\nu)}{\varepsilon A} [\langle T \rangle + (z - l_s/2)\langle \tau \rangle]_{z=0, l_s}, \quad (13)$$

where e and ε are the transducer effective piezoelectric and dielectric constants along the z -direction (i.e. the direction of incidence of the radiation beam), respectively, L (A) is the transducer thickness (area), α_T and ν are the linear thermal expansion coefficient and the Poisson ratio of the sample, $\langle T \rangle$ is the sample z -averaged temperature, namely,

$$\langle T \rangle = \frac{1}{l_s} \int_0^{l_s} dz T_s(z, t), \quad (14)$$

and $\langle \tau \rangle$ is the sample averaged temperature gradient,

$$\langle \tau \rangle = \frac{12}{l_s^3} \int_0^{l_s} dz (z - l_s/2) T_s(z, t). \quad (15)$$

The first term of eq. (13) represents the contribution to the PZT signal coming from the sample thermal expansion, as previously mentioned, whereas the second term is due to the sample buckling resulting from the temperature gradient set in the sample. Detailed calculations by Jackson and Amer [61] showed that for both thermally thin and thermally thick samples the output voltage from the PZT crystal is proportional to the optical absorption coefficient, for transparent samples, and depends on the

sample's thermal properties, incident radiation power, and modulation frequency as [61]

$$V \sim \frac{\alpha_T P_L}{(\rho c)_s I_s \omega} \quad (16)$$

Physically, P_L/ω is the incident power per cycle, $(\rho c)_s^{-1}$ represents the conversion of the incident energy into a temperature rise, and α_T transforms this temperature rise to a strain. The ω^{-1} frequency dependence for thermally thin and thick samples is a consequence of the fact that piezoelectric detection responds to absorption of radiation by the entire sample, and not merely within a thermal diffusion length as in thermal wave detection of photoacoustics. Jackson and Amer [61] were able to measure absorption coefficients as low as 10^{-5} cm^{-1} for didymium glass samples in the 5800 \AA region, thereby demonstrating the high sensitivity of PZT detection.

2.3.2. Photothermal beam deflection (PBD)

This is a non-contact technique originally proposed by Boccarda et al. [62, 63] and Fournier et al. [64]. It is based on the concept of beam deflection by thermally induced changes in the refractive index (mirage effect). In fig. 8 we show schematically a typical PBD experimental configuration. The absorption of a modulated pumping beam followed by the diffusion of the deposited heat causes a gradient in the refractive index in a thin layer of gas (or liquid) adjacent to the sample surface. This refractive index can be probed by a second beam (say, tangential to the sample surface) and one can relate its deflection, when crossing the illuminated region of length L , with the sample surface temperature. As the increase of the sample surface temperature depends on the optical absorption coefficient of the sample as well as on its thermal properties, both spectroscopic and thermal characterization studies can be conducted by measuring the deflection of the probe beam.

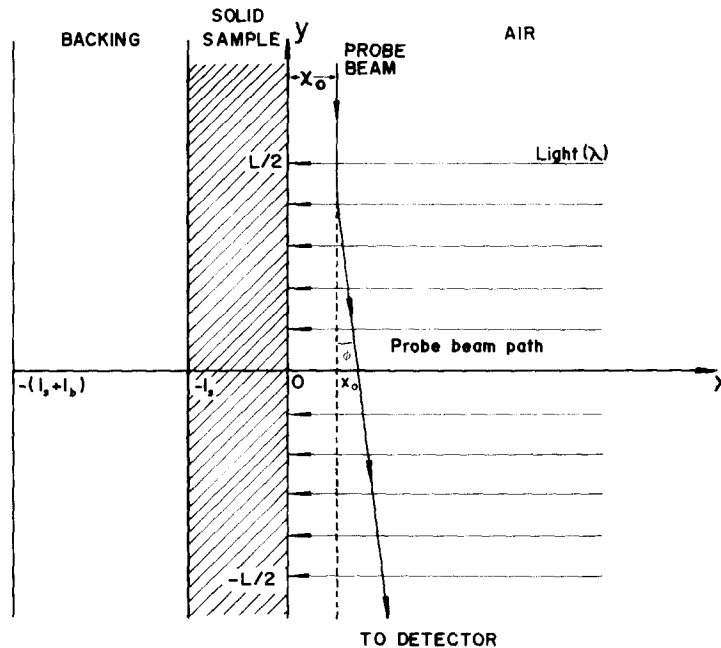


Fig. 8. Typical PBD experimental configuration.

Detailed theoretical models for the description of the PBD spectroscopy have been discussed in the literature [65–67]. The essential features of the PBD signal can be understood, however, using the simple one-dimensional model as depicted in fig. 8. For further reference on the one-dimensional model of PBD detection we refer to the work of Mandelis [67]. Denote by $T_g(x, t)$ the temperature fluctuation in the gas adjacent to the sample resulting from the absorption of the modulated pumping beam. This is found by solving the thermal diffusion equation for the solid–gas system of fig. 8, similarly to the PA case. Assuming that the probe beam passes through the gas parallel to the sample surface at a distance x_0 from the surface, it will be deflected by an angle ϕ from its original path. For small deflections, ϕ is given by [62, 65, 67]

$$\phi = \frac{L}{n} \left(\frac{\partial n}{\partial T} \right)_{T_0} \left(\frac{\partial T_g}{\partial x} \right)_{x=x_0}, \quad (17)$$

where

$$T_g(x, t) = \theta e^{-\sigma_g x} e^{j\omega t} \quad (18)$$

is the temperature distribution in the gas, and n_0 is the refractive index of the gas at the ambient temperature T_0 . The deflection is experimentally measured by means of position-sensitive diode detectors. As the signal decreases exponentially with the probe beam offset x_0 it is favorable, for enhanced signal-to-noise ratio, to perform experiments with the sample immersed in a non-absorbing liquid. In liquids $\partial n/\partial T$ is typically $10^{-4} \text{ }^\circ\text{C}^{-1}$, whereas for air at 20°C , $\partial n/\partial T \sim 10^{-6} \text{ }^\circ\text{C}^{-1}$. We also note that only the change of the refractive index with temperature is being considered. In general, the refractive index is a function of both temperature and pressure. However, it can be shown [66] that, unless one uses very high modulation frequencies ($\sim\text{MHz}$), the pressure contribution is negligible.

The PBD technique has been applied to the absolute measurement of the optical absorption coefficients of thin films, solids, liquids and gases [62–68] and more recently to a quite diverse class of problems ranging from imaging and scanning microscopy to flow-velocity measurements in flames. Further examples of PBD are discussed in the next section. Being a non-contact technique, PBD offers great advantage in monitoring ultrasonic testing and imaging and in remote sensing of samples exposed to chemically or thermally hostile environments, or confined to an environment not to be contaminated.

2.3.3. Photothermal radiometry and other remote sensing techniques

Photothermal radiometry (PTR) is another example of a non-contact technique consisting basically in the monitoring of the changes induced in the thermal radiation emission of a sample as it is periodically heated by the absorption of chopped light. It was originally proposed by Kanstad and Nordal [69–72]. In fig. 9a we show a typical PTR experimental arrangement, in which the monochromatic light from a tunable light source, after being mechanically chopped, illuminates the sample. The light absorbed by the sample is converted, partly or completely, into heat. Since the heat so deposited depends upon the optical absorption coefficient β of the sample, one should then expect that the induced changes in the total thermal radiation of the sample also depend on β . The thermal radiation from the illuminated area is collected by an appropriate optical system and focused on an infrared detector. To prevent the scattered radiation from the incident (driving) beam from reaching the thermal radiation detector, a simple optical filtering system is usually coupled to the infrared optical collecting system. The analog signal from the detector is then fed into a tunable (lock-in) amplifier,

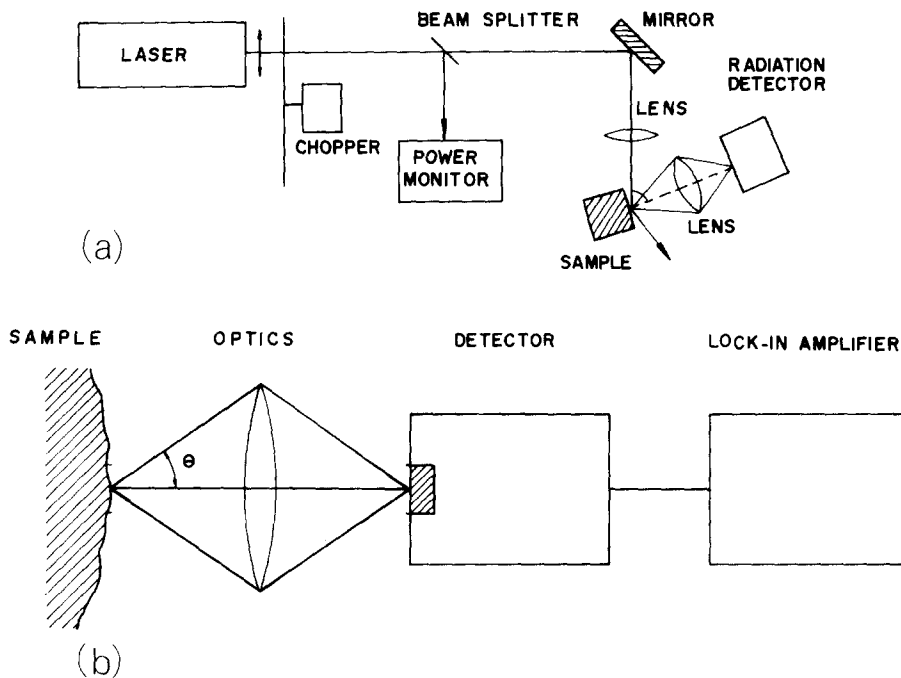


Fig. 9. (a) Experimental configuration for PTR measurements at the front surface. (b) Sample-detection system arrangement used in PTR experiments.

whose output is recorded as a function of incident light wavelength. In this way, PTR spectra are obtained and found to correspond to the optical absorption spectra.

Even though the above description is basically centered on a chopped continuous-wave (CW) illumination followed by a lock-in detection, PTR studies can also be performed using pulsed excitation with boxcar or transient detection. This latter aspect of PTR spectroscopy represents one of the great advantages of this technique over the otherwise similar PA spectroscopy. The photothermal emission occurs immediately upon thermalization of the absorbed energy (typically within $\sim 10^{-8}$ – 10^{-12} s) and, therefore, the use of pulsed excitation allows us to perform spectral studies of transient phenomena with a time resolution essentially determined by the response time of thermal radiation detectors ($\sim 10^{-7}$ s).

The theoretical description of the PTR signal, for both CW and pulsed excitation, has been discussed by Santos and Miranda [73] and Tom et al. [74]. In particular, it has been found in ref. [73] that pulsed PTR techniques allow surface and bulk spectral absorption coefficients to be distinguished and measured separately. This possibility has been later demonstrated experimentally by Tam and coworkers [75–77]. The theory of the PTR signal resembles that of RG for PA spectroscopy in the sense that the one-dimensional model for the heat flow in the sample-gas system of fig. 9 is also used to determine the sample surface temperature fluctuation δT . As in the PA case, this temperature fluctuation depends on the optical and thermal properties of the sample, as well as on the modulation frequency. As a result of this surface temperature fluctuation, the thermal radiation emitted by the sample also fluctuates according to the Stefan-Boltzmann law ($W = \epsilon\sigma T^4$) as

$$\delta W = 4\epsilon\sigma T_0^3 \delta T, \quad (19)$$

where $\sigma = 5.67 \times 10^{-12} \text{ W cm}^{-2} \text{ K}^{-4}$ is the Stefan–Boltzmann constant, ε is the sample emissivity, and T_0 is the d.c. surface temperature. The actual PTR signal sensed by the detector is obtained as follows. Referring to the sample–detection system in fig. 9b, the observed area of the sample, assumed to be a Lambertian radiator, is determined from the detector area A and the collecting angle θ . The PTR signal for a broad-band detector over the entire thermal radiation spectrum may then be written as

$$S = 4\varepsilon\sigma T_0^3 A \sin^2\theta \delta T. \quad (20)$$

In general, however, the use of broad-band thermal detectors is limited to strong signals. In the case of weak signals, more sensitive semiconductor detectors (usually, nitrogen-cooled) are recommended. These detectors have sensitivities in a given spectral region $\Delta\lambda$ around a detection wavelength λ_d . If one chooses the detector such that λ_d is close to the maximum contrast wavelength, λ_m , given by the displacement law, $\lambda_m T = 1410.5 \text{ K } \mu\text{m}$, an approximate expression for the PTR signal is then

$$S = \varepsilon A \sin^2\theta T(\lambda_d) R(\lambda_d) \frac{\partial W}{\partial T}(\lambda_d) \Delta\lambda \delta T. \quad (21)$$

In eq. (21), $T(\lambda_d)$ is the spectral transmission of the collecting optics, $R(\lambda)$ is the spectral sensitivity of the detector, and $\partial W/\partial T$ is the temperature derivative of Planck's radiation function, namely,

$$\frac{\partial W}{\partial T} = \frac{2\pi k_B c}{\lambda^4} \left(\frac{hc}{\lambda k_B T} \right)^2 e^{hc/\lambda k_B T} (e^{hc/\lambda k_B T} - 1)^{-2}. \quad (22)$$

For further discussions on several experimental aspects of PTR detection we refer the reader to a recent review by Kanstad and Nordal [78].

The above discussion shows that, regardless of the detection scheme adopted, the PTR signal is always proportional to the surface temperature fluctuation δT . For example, in the important case of an optically opaque sample ($\beta \gg 1$), such that the diffusion coefficient $(\pi f/\alpha_s)^{1/2}$ is much greater than the optical absorption coefficient, δT is given by [73]

$$\delta T \approx \frac{\beta I_0}{2\pi f \rho_s c_s} e^{j\omega t}. \quad (23)$$

In other words, the PTR signal becomes proportional to the absorption coefficient and, consequently, spectroscopic studies as a function of the illumination wavelength can be carried out. In contrast, at smaller modulation frequencies or for strongly absorbing samples, such that the optical absorption coefficient is much greater than the thermal diffusion coefficient, the PTR signal reduces to

$$\delta T \approx \frac{I_0}{(2\pi f k_s \rho_s c_s)^{1/2}}. \quad (24)$$

In this case, the signal becomes independent of the absorption coefficient but varies inversely proportionally to the sample's thermal effusivity. Thus, by varying the modulation frequency, one can probe the thermal properties of the sample through the changes of its thermal properties, similarly to the PA depth-profile analysis. PTR detection has been applied to both spectroscopic as well as non-spectroscopic studies. Examples of the former go back to the earlier works of Kanstad and Nordal

[71–79] for the case of powders, biological specimens, etc. In the case of non-spectroscopic studies, the applications range from the analysis of surface layers and coatings [80–83] to the inspection of internal structures of materials [84–89]. This latter thermal-wave imaging aspect of PTR, originally developed by Busse, has been recently reviewed by Reynolds in the context of industrial materials applications.

Apart from the PTR and PBD techniques previously discussed, some other remote sensing techniques have also been proposed. These include the interferometric detection [90–95] of gas displacement in closed cells as well as of the thermoelastic displacement of the sample surface due to the modulated heating, and thermal lensing detection [96–100]. The latter detection technique dates back to the work of Leite et al. [96], who were the first to show that monitoring the self-defocusing of an excitation beam due to the photothermal effect offers a sensitive tool for spectroscopic studies. Self-defocusing, instead of self-focusing, generally occurs because the refractive-index gradient produced by the heat gradient due to the absorption of an excitation beam, is usually negative.

2.3.4. Photopyroelectric detection

To conclude this section we review a second example of a contact-type photothermal detection technique, namely, the so-called photopyroelectric (PP) detection. It is based on the use of pyroelectric thin films to detect the temperature rise in the sample when it is exposed to modulated heating. In a pyroelectric material a temperature fluctuation induces an electrical current proportional to the rate of change of its average heat content. The addition of pyroelectric detection to the already rich arsenal of modern photothermal techniques was recently revived by Coufal [101] and further explored by Mandelis and coworkers [102, 103] and other authors [104, 105]. For a recent review on PP detection we refer to the work by Coufal [106], where further references to the literature can be found.

In fig. 10a we show a typical experimental arrangement of the PP technique. It consists of using a thin pyroelectric film (e.g. polyvinylidene difluoride, PVF₂) in intimate contact with the sample, on which a monochromatic light beam whose intensity is sinusoidally modulated at a frequency ω is incident. Following the absorption of the incident light, the nonradiative deexcitation processes within the sample cause a temperature fluctuation which through heat diffusion reaches the pyroelectric film. As a result of this temperature fluctuation the pyroelectric material changes its polarization and an electric current is induced in the detector. Denoting by $T_d(x, t)$ the temperature fluctuation in the pyroelectric detector resulting from the modulated heat deposition in the sample, and by ΔT its spatially averaged temperature fluctuation, namely,

$$\Delta T = \frac{1}{l_d} \int_0^{l_d} dx T_d(x, t), \quad (25)$$

the induced current in the pyroelectric film is [107]

$$i_p = -pA \frac{d\Delta T}{dt}, \quad (26)$$

where p is the pyroelectric constant of the material and A is the detector area. Equation (26) is the basic equation for the pyroelectric detection technique. It relates the current i_p sent by the detector to the photothermal effect at the sample through the averaged temperature fluctuation ΔT .

Actually, for a non-ideal, i.e. real, sensor the observed signal depends on the impedance of the detector and electronic circuitry used. The equivalent circuit for the pyroelectric detector is that of an

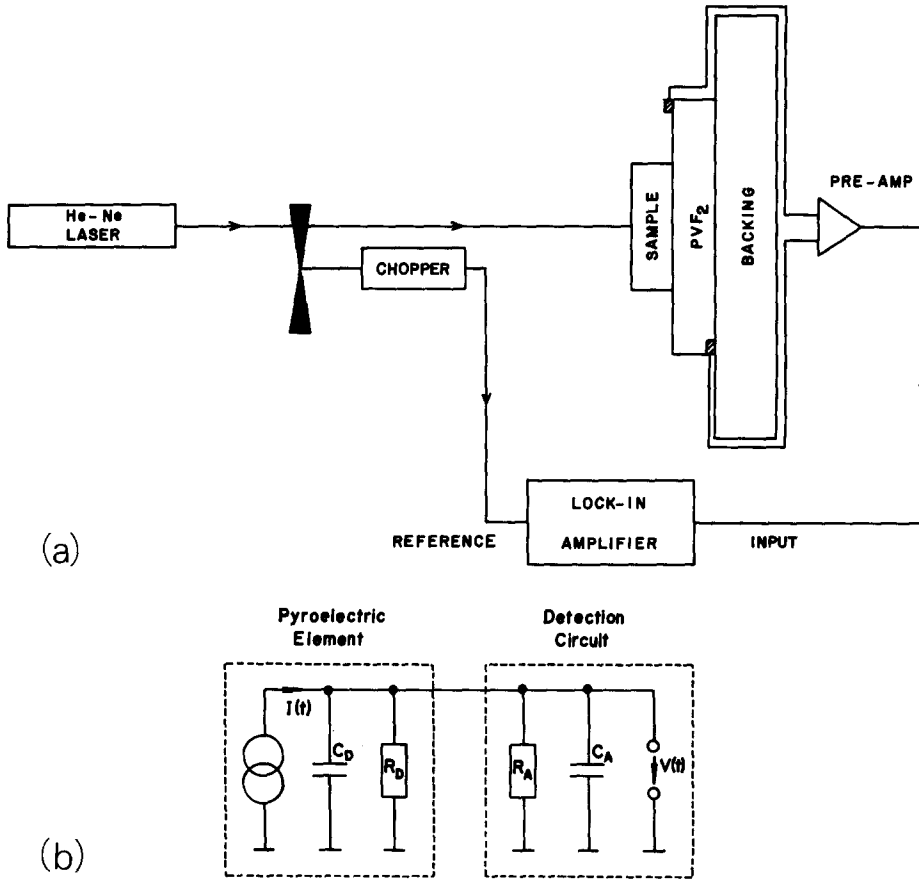


Fig. 10. (a) Typical experimental arrangement for PP detection. (b) Equivalent electronic circuit involved in pyroelectric voltage detection.

ideal current source i_p given by eq. (26) in parallel with a capacitance C_d formed by the electrodes and the pyroelectric element, and a leakage resistance R_d due to the dielectric losses. The signal from the pyroelectric element is detected by a voltage detection circuit with an input capacitance C_a in parallel to a coupling resistance R_a . This equivalent circuit involved in pyroelectric voltage detection is shown schematically in fig. 10b. The output voltage V from the pyroelectric sensor, which is fed into a lock-in amplifier as depicted in fig. 10a, is related to i_p by

$$\frac{dV}{dt} + \frac{V}{\tau_E} = \frac{i_p}{C}, \quad (27)$$

where $C = C_d + C_a$ and $R = R_d R_a / (R_d + R_a)$ are the effective capacitance and resistance of the equivalent circuit, and $\tau_E = RC$ is the electronic time constant. For a sinusoidally varying temperature fluctuation, eqs. (26) and (27) yield

$$V = \frac{-j\omega p R A \Delta T}{1 + j\omega \tau_E} e^{j\omega t}. \quad (28)$$

PP detection for spectroscopic studies was originally used by Coufal [101] and Mandelis [102]. Examples of non-spectroscopic applications of PP detection include thermal diffusivity measurements [104, 105, 108, 109], PP detection of phase transitions [110], photovoltaic conversion efficiency of solar cells [111], and PP scanning microscopy [112]. Further uses of PP detection will be discussed in the remaining sections.

3. Depth-profile analysis and microscopy

As already mentioned in the previous section, one of the important features of the PA technique, which was soon recognized, regards the potentiality of this technique to detect subsurface variations in both optical and thermal properties of a sample. These studies are called PA imaging and are essentially classified into two categories. If little lateral resolution is required, so that the PA imaging is mainly concerned with variations of the sample properties along its thickness, the technique is called PA depth profiling. The depth-profile analysis is performed by measuring the PA signal amplitude and phase as a function of the modulation frequency. As shown in the previous section, the PA signal is sensitive only to the heat generated within one thermal diffusion length $\mu = (\alpha/\pi f)^{1/2}$ beneath the sample surface. Here, α is the sample thermal diffusivity and f is the modulation frequency. Thus, at high modulation frequency, information about the sample near the surface is obtained, while at low modulation frequency the PA signal comes from deeper within the sample. If, however, high lateral resolution is required, the PA imaging is called PA microscopy. In this case one records the PA signal as the focused pumping beam spot is scanned along the sample surface.

The potentialities of PA depth-profile analysis were originally demonstrated by Adams and Kirkbright [113] for the simple case of a two-layer sample consisting of a top transparent layer of thickness l on an optically thick substrate. The specific example used by these authors to illustrate the PA depth-profile capability was that of polymer coatings on copper substrates. For this two-layer system, using the thermal diffusion model of section 2, Adams and Kirkbright [113] have shown that the PA signal is given by

$$S = \text{constant} \cdot \frac{e^{-la}}{f} \cos(\omega t - la - \pi/4), \quad (29)$$

where $a = (\pi f/\alpha)^{1/2} = \mu^{-1}$ is the thermal diffusion coefficient of the non-absorbing top layer. It follows from eq. (29) that the presence of a nonabsorbing top layer decreases the amplitude of the PA exponentially, $\exp[-la(\pi f/\alpha)^{1/2}]$ as a function of \sqrt{f} , and introduces a phase lag $\phi = la$, varying linearly with \sqrt{f} . The value of $l/\sqrt{\alpha}$ for the top layer can then be obtained either by a semilog plot of the PA amplitude versus \sqrt{f} or by a linear plot of the PA phase versus \sqrt{f} . Adams and Kirkbright [113] have tested this by comparing the values of l so obtained with the ones obtained by gravimetric measurements for several polymer-coated copper samples.

The PA depth-profile technique can provide not only information about the thickness of a surface layer, the thermal diffusivity of a coating, or irregularities below the surface, but also about depth-dependent spectral features. A good example of this latter case is the modulation frequency dependence of the visible PA spectra of an apple peel or of a spinach leaf reported by Rosencwaig [5] and Adams and Kirkbright [114], respectively. At a relatively high modulation frequency (e.g., $f \approx 300$ Hz, $\mu \approx 10$ μm), the PA spectrum corresponds to the optical absorption by the top cuticle layer

of the leaf sample, whereas at low modulation frequency (e.g., $f \approx 30$ Hz, $\mu \approx 33$ μ m), the PA spectrum corresponds to the absorption of both cuticle and pigment layers. Further examples of PA depth profiling of layered samples have been reported in the literature. These include the study of layered tape [115], color photographic films [116], chemically discolored ZnSe [117], in vivo dermatological applications [118], as well as distribution of pigments in lobster shells [119]. Generalized theories of thermal wave propagation in layered structures have been published by Iravani and Wickramasinghe [120], Baumann and Tilgner [121], Aamodt and Murphy [38] and Cesar [39].

The above outlined modulation frequency scanning depth-profile analysis presents, however, some experimental difficulties due to a poor signal-to-noise ratio at high modulation frequencies. To overcome such difficulty a single-frequency phase-resolved method (PRM) has been proposed. This method was independently proposed by Anjo and Moore [122] and O'Hara et al. [123] in the context of biological samples, and by Cesar et al. [124, 125] for solid samples. The basic idea of PRM may be summarized as follows. Let us consider a typical PA arrangement in which heat is generated within the sample due to the absorption of chopped radiation. For the sake of the argument, we further assume that the sample is made of two layers of materials A and B, with material A facing the gas phase of the PA cell. At a fixed modulation frequency, the acoustic signal detected at the microphone is the resultant of the contributions generated in both constituents A and B. As component B is beneath A there should exist a time lag between the signals arising from A and B due to the difference in the corresponding thermal diffusion times. This difference in the time to reach the gas phase produces a phase shift ϕ between the two signals.

Thus, the actually observed signal S may be viewed as the resultant of two vectors (whose lengths S_A and S_B correspond to the signals from A and B, respectively), with an angle ϕ between them. This means that once the angle ϕ is known, by varying the phase by 90° , say, with respect to the signal S_A , one should observe only the contribution of component B, and vice versa. In other words, by measuring the phase variation of the PA signal of a composite sample one may, in principle, single out the contribution of the different constituents at different locations. The different subsurface layers are then identified in the PRM by the transit time of the heat generated at a single modulation frequency.

From the experimental point the spectrum may be phase-resolved as follows. We record the in-phase (S_0) and out-of-phase (S_{90}) signals of our sample as a function of the incident radiation wavelength. The spectrum at a given phase ϕ is written in terms of $S_0(\lambda)$ and $S_{90}(\lambda)$ as (cf. fig. 11)

$$S(\lambda) = S_0(\lambda) \cos \phi + S_{90}(\lambda) \sin \phi . \quad (30)$$

By a computer-aided scanning of the phase ϕ of eq. (30) we then search for the phase ϕ' at which, say, the signal from the inner layer S_B is in quadrature. In this case only the signal S_A of the outer layer is present and the phase ϕ_B , which is in quadrature to ϕ' , is readily obtained. We next search for the phase ϕ'' in which only the signal S_B of the inner layer is present, which in turn gives us the phase ϕ_A (in quadrature to ϕ'') of the outer layer signal.

The phase-resolved method may be applied preferably when the dynamical range in modulation frequency is limited by experimental conditions. Various examples of this detection technique for PA microscopy have been reported. Depth profiles of ferromagnetic layered samples using phase monitoring of the PA-detected ferromagnetic resonance were studied by Cesar et al. [124, 125] and Netzelmann et al. [126]. Neri et al. [127] have described the use of PRM for carrying out time evolution depth analysis of biological layered samples. In particular, the usefulness of PRM was demonstrated for monitoring the action of a herbicide in the degradation of a green leaf. Phase-resolved data for an intact

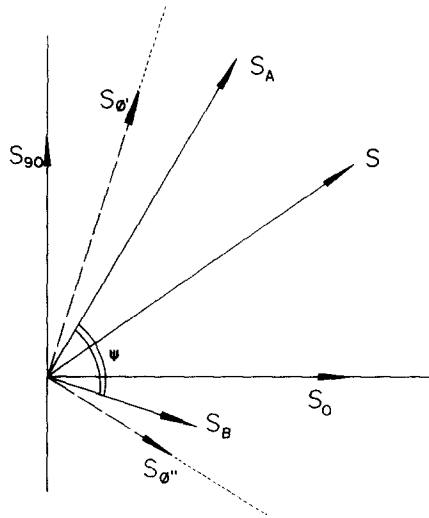


Fig. 11. Vectorial representation of the PA signals of two different layers, S_A and S_B , in terms of the in-phase and quadrature signals, S_0 and S_{90} , respectively.

coffee leaf [127] are shown in fig. 12. After recording the two spectra at quadrature, S_0 and S_{90} , at a fixed modulation frequency of 25 Hz, the signal at a given phase ϕ was computed using eq. (30). In fig. 12 we show the in-phase spectrum of the leaf, exhibiting the characteristic absorption bands of the waxy cuticle, carotenoids and chlorophyll. From figs. 12c and 12d we note that the spectra corresponding to the pigment layers and the cuticle could be singled out at the phases $\phi = -30^\circ$ and $\phi = 80^\circ$, respectively.

The PR method is applicable not only to the case of layered samples as illustrated above but can also be used for resolving the spectra of absorption centers that are homogeneously distributed in given matrix. This has recently been demonstrated by Lima [128] using soda–lime silica glass samples doped with binary mixtures of CuO, CrO, and CoO oxides. For a sample consisting of two absorption centers A and B, centered at the wavelengths λ_a and λ_b , respectively, that are homogeneously distributed in the matrix, the phase lag, if any, between the signals from A and B is attributed to the difference between the non-radiative relaxation time and the characteristic diffusion time of these two centers. The influence of the non-radiative relaxation time on the RG model for the PA signal has been discussed by Mandelis and Royce [129]. For a thermally thick sample, the variable component of the PA phase can be written as

$$\phi = \tan^{-1}(\omega\tau) - \tan^{-1}\left(\frac{1}{1 + (2\omega\tau_\beta)^{1/2}}\right), \quad (31)$$

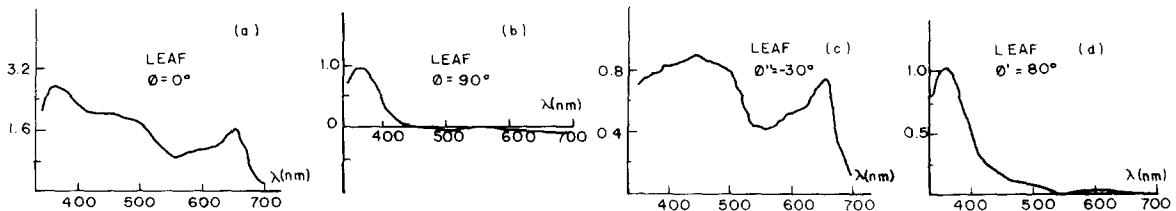


Fig. 12. PRM applied to a coffee leaf. (a) In-phase signal S_0 . (b) Quadrature signal S_{90} . (c) Pigment spectrum resolved at $\phi = -30^\circ$. (d) Cuticle spectrum resolved at $\phi = 80^\circ$. (After Neri et al. [127]).

where $\tau_\beta = (\beta\alpha_s)^{-1}$, with α_s being the thermal diffusivity of the sample and β its optical absorption coefficient, and τ is the non-radiative relaxation time. The first term in eq. (31) corresponds to the non-radiative relaxation contribution to the PA phase, while the second one is due to the thermal diffusion within the optical absorption depth β^{-1} . Thus, for absorption centers with different absorption strengths and having different non-radiative relaxation times there may exist a time lag between their contributions to the PA signal, and we may, in principle, single out their spectra by the phase lag method outlined above.

The potentiality of the PA technique for subsurface imaging of irregularities, flaws, etc. was originally demonstrated by Wong et al. [130] and other authors [131–138]. Further references can be found in the book by Ash [139]. PA microscopy is a rapidly expanding area because of its potential applications in thin-film technologies, medical diagnostics, and non-destructive testing, to name a few examples. In addition to gas–microphone detection, several other detection techniques have been used in photothermal microscopy. These include PZT [140–145], PBD [62, 65, 146, 147], and PTR [84–89] detection, as well as photothermal surface displacement [148] measurements.

Photothermal microscopy consists basically of generating a localized periodic heating in a sample, due to the absorption of an intensity modulated energetic beam (e.g. laser or electron beam), and scanning the heating position across the sample. The thermal waves resulting from the absorption of the periodic incident beam propagate from the heated regions and undergo reflection and scattering when they encounter regions of different thermal and geometrical characteristics. In this way, as the heating beam is scanned across the sample any surface or subsurface change in the thermal characteristics of the sample can be monitored as a change in the thermal wave signal.

In the first report on PA imaging by Wong et al. [130], an Ar ion laser, modulated at a frequency between 50 and 2 kHz, was focused onto a silicon carbide ceramic sample used in turbine blades. They found that any surface and subsurface microstructure could be detected by changes in the PA signal when the chopped laser beam was scanned across the sample. These authors have later shown [149] that the spatial resolution of PA microscopy is essentially dictated by the thermal diffusion length μ of the sample. For thermally more conductive samples, such as Al and Si, $\mu \approx 50 \mu\text{m}$ at $f = 10 \text{ kHz}$, while for thermally less conductive materials, such as SiO_2 and polymers, $\mu \approx 5 \mu\text{m}$ to $2 \mu\text{m}$ at the same modulation frequency. Spatial resolution of about $2 \mu\text{m}$ has been reported by Luukkala and Penttinen [131] for the case of photolithographic masks using a He–Ne laser chopped at 1 kHz. Both the PA signal amplitude and phase have been used to map subsurface features. However, it was demonstrated by Rosencwaig and Busse [140] that the PA phase image is usually more valuable than the PA amplitude image because the former is much less dependent upon optical absorption variations. Improvements in the signal-to-noise ratio in PA microscopy have been suggested by Coufal et al. [150] by using a spatial multiplexed technique, e.g. via Hadamard transformations.

In fig. 13 we show a typical experimental arrangement for PT microscopy using gas–microphone detection, as discussed by Busse [132]. The scanning of the focused laser beam is carried out using a voltage-controlled rotating mirror. The pumping laser beam used in Busse's experiment was a 5 W CO_2 laser and the sample studied was an Al sample provided with two 3 mm diameter holes hidden at 0.3 mm and 0.6 mm below the surface. In fig. 14 we show the output microphone signal amplitude and phase, at 10 Hz modulation frequency, as a function of the sample coordinates while the laser beam is swept over the sample. The two maxima in the phase curve of the PA signal (solid line) occur where the holes are and are easily correlated with the subsurface defects. In contrast, the amplitude of the PA signal (dashed line) exhibits a third maximum, thereby making its interpretation more difficult. The reason for this lack of resolution in the amplitude of the signal was attributed by Busse [132] to the fact

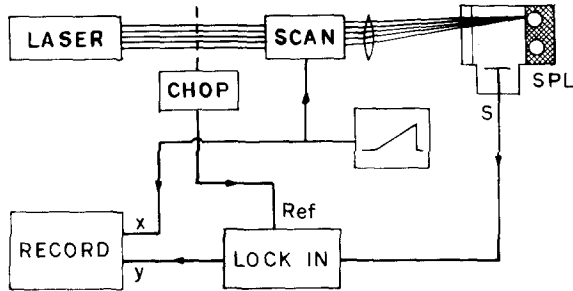


Fig. 13. Experimental arrangement to record phase and amplitude of the photoacoustic signal S as a function of sample coordinate. The sample is indicated by SPL.

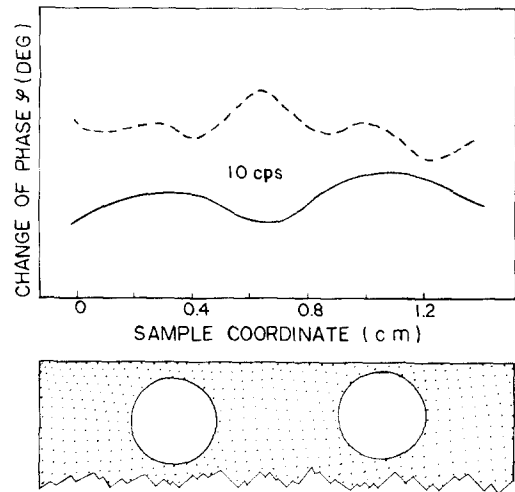


Fig. 14. Change of phase (solid line) and amplitude (dashed line) when the CO_2 laser beam is scanned over the Al sample. The chopping frequency is 10 Hz. The two maxima in the phase curve occur where the holes in the sample are (bottom). They correspond to the weaker maxima in the amplitude scan. (After Busse [132])

that different sample thicknesses close to the thermal diffusion length give rise to the same signal amplitude. Thus, to unambiguously monitor the sample thickness it is more useful to monitor the PA phase rather than its amplitude if the sample thickness is comparable to or larger than the thermal diffusion length.

In addition to the different PT detection techniques previously mentioned, the recently developed photopyroelectric (PP) technique has been proposed by Faria et al. [112] as another method to the already rich arsenal of thermal wave microscopy techniques. The difference between the proposed pyroelectric and the conventional gas-microphone detections rely basically on the fact that in the former the sample is mounted directly onto the pyroelectric sensing element as discussed in section 2; i.e., it is an open-cell configuration rather than a closed-cell one as in the gas-microphone case. Faria et al. [112] were able to demonstrate the usefulness of PP microscopy for monitoring both surface and subsurface defects using as a testing sample a Si wafer $600 \mu\text{m}$ thick in which a $250 \mu\text{m}$ wide slot was machined in one of its surfaces. The pumping laser beam used by these authors was provided by a 4 mW He-Ne laser. The laser beam was focused on the sample by means of a cylindrical lens, providing a focused strip less than $50 \mu\text{m}$ wide. In fig. 15 we show the PP signal as a function of the heating laser beam at a modulation frequency of 28 Hz. The laser beam was focused on the smooth surface of the silicon wafer, to simulate a subsurface defect. As seen in fig. 15 a clear maximum is exhibited in the PA signal amplitude as the beam is scanned over the region of the defect.

Faria et al. [112] have also investigated whether the proposed PP microscopy could not only point out the location of the defect but also give us information about the physical nature of the defect, as manifested, for instance, by a change in the thermal diffusivity in the defect region. To answer this question these authors have performed a lateral heating experiment [112] using a $250 \mu\text{m}$ thick Si wafer sample in which a thin Cu strip 5000 \AA thick and $200 \mu\text{m}$ wide was deposited in one of its surfaces.

A similar PP imaging experiment using electron beam heating rather than light beam heating has been reported by Bauman et al. [151].

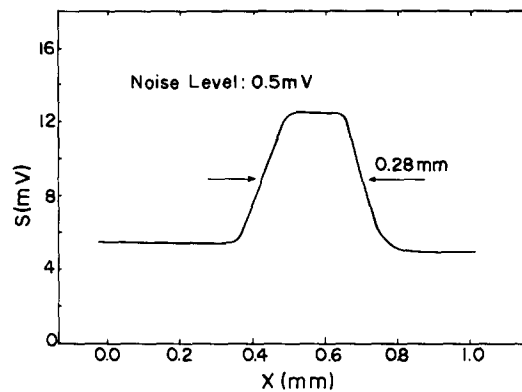


Fig. 15. Photopyroelectric image of a subsurface defect consisting of a $250\ \mu\text{m}$ wide slot on a $600\ \mu\text{m}$ thick silicon wafer at 28 Hz. The smooth surface of the wafer is facing the laser beam. (After Faria et al. [112])

For further references on PT microscopy we refer to the papers by McDonald [34] and Thomas et al. [152], where other aspects of PT microscopy as applied to nondestructive testing of materials are discussed.

4. Microwave spectroscopy

The use of PA detection was shown to be of great advantage in spectroscopic studies in a number of solid-state, chemical, and biological systems. Most of these studies were originally performed in the UV-visible region of the electromagnetic spectrum. Such studies, however, can be performed at any wavelength provided the sample one is dealing with absorbs the radiation at the incident wavelength. The first indication of the feasibility of using PA detection for microwave spectroscopy came from the experiment of Diebold and McFadden [153] on gaseous O_2 . Since then, a number of authors [154–162] have applied the PA detection to perform microwave absorption studies of a wide range of materials. These include the PA detection of ferromagnetic resonance (FMR) of metallic [154, 155] and non-metallic [156] samples, spin wave resonance in thin metallic films [157], and paramagnetic resonance (EPR) in organic and inorganic substances [158–161].

The use of the PA method for detecting ferro- and paramagnetic resonances in solids, including a comparison between the PA and the more conventional (thermal and electronic) methods, have been reviewed by one of us [162]. In these experiments the measurements are usually performed in a conventional X-band EPR spectrometer by integrating the PAS cell into the microwave cavity. Figure 16 shows the setup for photoacoustic EPR and FMR detection. A klystron is used as the source of the microwave, which is chopped by applying square pulses to the reflector [162]. The sample to be studied is placed in the PA cell and is positioned at the shorter end of the waveguide between the poles of an electromagnet. By chopping the microwave power absorbed by the ferromagnetic or paramagnetic sample inside the PA cell, the increase in temperature of the sample during resonances cause pressure fluctuations in the surrounding gas, which are measured by a microphone. The PA method of detection is very similar to the thermal detection method in which to detect the EPR or FMR spectrum a sensitive thermometer is attached to the sample [163, 164].

Figure 17 shows construction details of two different types of photoacoustic cell. The cell on the left allows one to measure the actual microwave magnetic field inside the cavity, which provides the

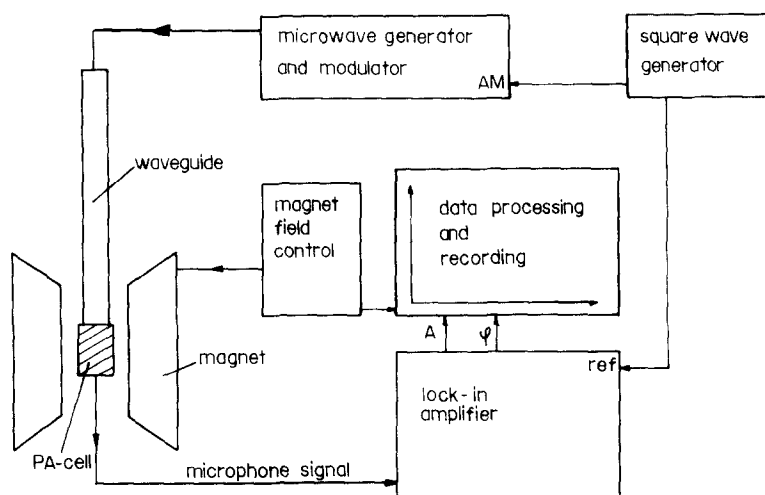


Fig. 16. Block diagram of the experimental apparatus used for photoacoustic FMR and EPR detection (after Vargas [162]).

necessary normalization factor for the PA signal from the samples [124, 125]. If the photoacoustically detected signal is normalized with respect to the actual microwave magnetic field it yields signals or resonance curves which are proportional to the signals obtained by conventional (thermal and electronic) methods. This correspondence was observed by Cesar et al. [165]. This type of cell is particularly suited for phase-resolved measurements in a “thermal transmission” arrangement [124, 125]. This arrangement allows simultaneous recording of the PA and conventional EPR spectrum

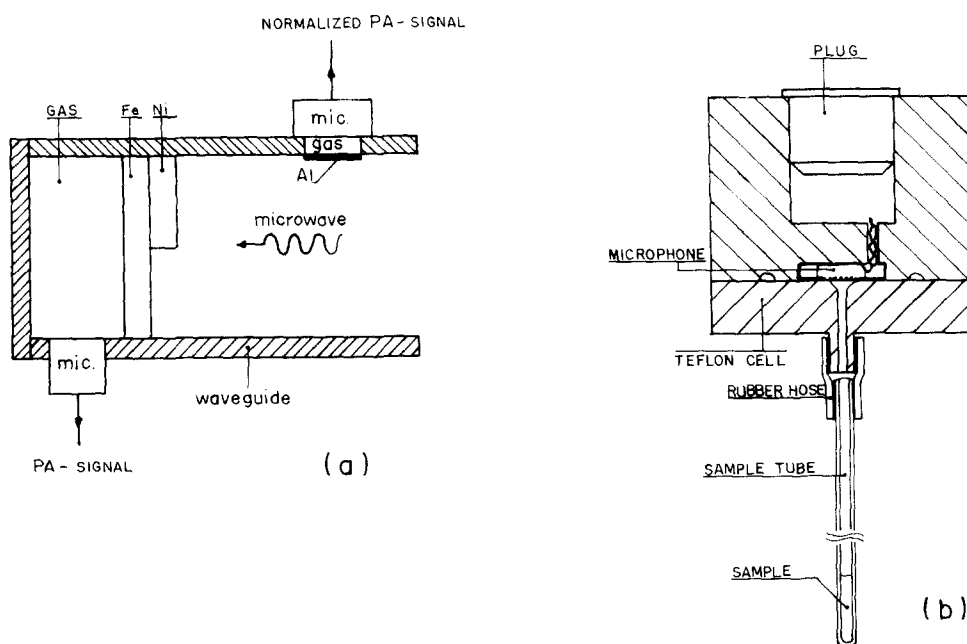


Fig. 17. Construction details of PA cells. The cell (a) is machined in a waveguide short. The sample is followed by a gas cell in which a miniature microphone is mounted on one of its walls. A second cell was mounted in one of the waveguide's walls so that the actual microwave magnetic field H_0 could be measured (after Cesar et al. [124]). The cell (b) fits into a X-band cavity (after Netzelmann et al. [126]).

[159, 126]. The cell is located in the X-band cavity replacing the sample tube normally used in an EPR experiment.

Photoacoustic detection provides a unique opportunity to obtain FMR and EPR depth profiles that cannot be obtained using conventional techniques. This was first reported by Cesar et al. [124], who measured the phase-resolved variations of the PA detected FMR of a Ni-Fe layered sample, and by Netzelmann and Pelzl [166] on layered ferromagnetic tapes using frequency dependent PA detection. Other reports of PA detected FMR depth profiles have appeared [125, 126]. Phase-resolved data for Ni-Fe layered samples are shown in fig. 18. The lower part of the figure shows the in-phase and out-of-phase PA signal amplitudes corresponding to FMR in the artificial Ni-Fe sample. Based on these data at 10 Hz, amplitude spectra which correspond to other phase angle offsets ϕ were calculated with the relation $S(H) = S_0(H) \cos \phi + S_{90}(H)$ (see discussion in section 3), where $S_0(H)$ and $S_{90}(H)$ are the measured in-phase and out-of-phase components of the PA amplitude, respectively [125, 126]. At an angle $\phi = -60^\circ$ the PA-FMR amplitude reproduces the resonance in the iron layer and at $\phi = +80^\circ$ the resonance corresponds to that of the Ni foil. The depth position of the two layers can be determined from the observed relative magnitude of the phase lags in units of the thermal diffusion length. In the present case, as demonstrated by the authors [125, 126], the phase difference between the Ni and the Fe comes from the time the heat wave generated in the Ni foil needs to diffuse through the glue layer.

Netzelmann and Pelzl [166] obtained depth profiles from commercially available cassette recorder tapes. Three different products of BASF labeled as ferrochrome, chromium dioxide (CrO_2) and

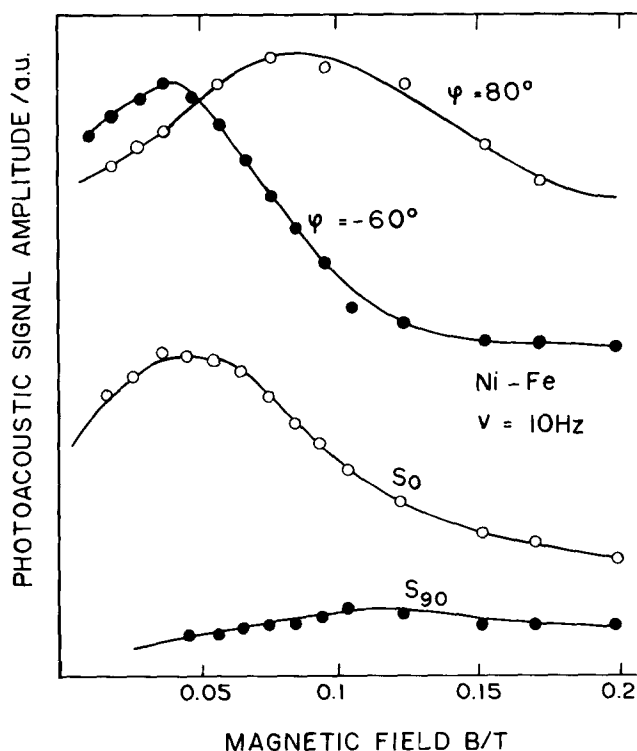


Fig. 18. Lower part: Magnetic field dependence of the in-phase component S_0 and the out-of-phase component S_{90} of the photoacoustically detected FMR signal from a Ni-Fe sandwich at 10 Hz. Upper part: Signal at two selected phase offsets ϕ deconvoluting the Fe resonance at 0.03 T and the Ni resonance at 0.08 T (after Netzelmann et al. [126]).

iron(III) oxide (Fe_2O_3) were investigated; the ferrochrome tape is composed of CrO_2 and Fe_2O_3 layers, exhibiting a structure as indicated in the inset of fig. 19. Tapes containing pure oxides have been used as reference samples to locate the resonances of chromium and iron using the conventional method. The amplitude and the phase angle of the PA-FMR signals of the iron oxide, chromium oxide and ferrochrome tapes were measured at different modulation frequencies. The upper curves of fig. 19 show the PA detected ferromagnetic resonance of a ferrochrome tape at five frequencies. A comparison of these curves with the conventional FMR absorption spectra of Fe_2O_3 (not shown) and CrO_2 (shown in the lower part of fig. 19) indicates that the PA detected spectra at the lowest and highest modulation frequencies correspond to the conventional FMR spectra of ferrochrome and CrO_2 , respectively. The observed phase angle changes were used to obtain an estimate of the thickness of the CrO_2 [166]. The depth resolution, which is a function of the thermal diffusivity of the material and the modulation frequency, was as low as $1\ \mu\text{m}$ in the case of the ferromagnetic tapes. As in the case of thermal detection using bolometric techniques [163, 164], PA detection is very sensitive at low temperature. This is because the specific heat of the crystal lattice falls rapidly as T^3 .

Vasson and Vasson [160] describe a cell for PA measurements between room and liquid helium temperatures. Absorption lines of several systems (DPPH , $\text{CuSO}_4 \cdot 5\text{H}_2\text{O}$, KTiF_4) were recorded between 300 and 4.2 K at 9.3 GHz. Some of the PA detected EPR spectra at different temperatures obtained in ref. [160] are shown in fig. 20. Observations of spin wave resonance (SWR) at liquid nitrogen were reported by Davies and Heath [157]. Although the sensitivity at room temperature is considerably less than that of field modulation detected spectra, there are considerable advantages to be gained by the use of PA detection, particularly when the linewidths become very large as in critical angle studies of SWR in thin films [167], and in PA detected EPR of high-spin ferritetraphenylporphyrin (Fe(III) TPP) [159]. Another advantage of photoacoustic detection of FMR or EPR absorption over

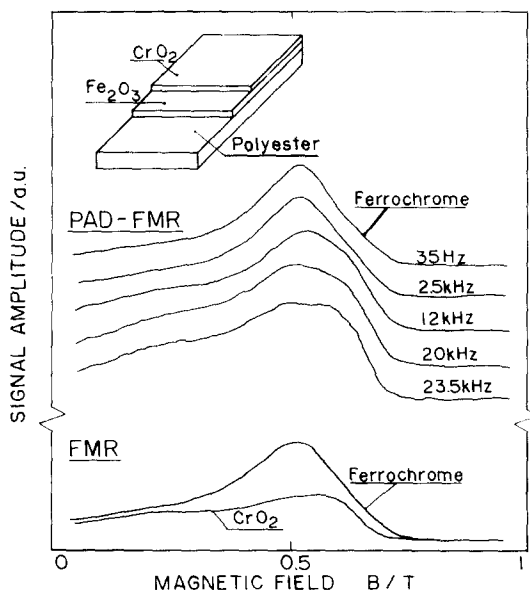


Fig. 19. Upper traces: Photoacoustic amplitude recordings of the FMR from a ferrochrome tape (BASF) at different modulation frequencies of the microwave power. Lower traces: FMR absorption of a ferrochrome tape and of a CrO_2 tape obtained by a conventional technique. In both cases the external magnetic field was oriented parallel to the sample surface. The inset shows the layered structure of the ferrochrome tape. (After Netzelmann et al. [166])

the more common field modulation diode detection is that, in the latter case, the observed spectra are usually displayed as the derivative of the absorption spectra, and this does not necessarily show the actual relative peak heights, linewidths and lineshapes [162, 167]. Photoacoustic detection produces the true absorption spectra, but must be regarded as a complementary technique at present, due to shortcomings of the signal-to-noise ratio techniques when compared with high-frequency field modulation techniques.

Other photothermal studies of FMR and EPR have also been reported. DuVarney et al. [168] obtained EPR spectra of CuSO_4 single crystals cemented to a PZT located inside the cavity of an X-band spectrometer. With 100 mW microwave power, 10 kG magnetic field modulated at 20 Hz, these authors obtained comparable signal-to-noise ratios for PT and conventional detections. However, at high modulation frequencies (about 10–100 kHz) the conventional detection produces higher sensitivity. Melcher and Arbach [169] reported on the use of pyroelectric sensors to detect the temperature rise associated with magnetic resonance absorption in thin films and layers of paramagnetic and ferromagnetic materials. The local variation of the ferromagnetic resonance absorption, scanning along the surface of ferromagnetic metallic films, was studied by Netzelmann et al. [170] using the photothermal beam deflection technique. Scanning of the probe beam provides a means to obtain one-dimensional FMR images. As demonstrated by the authors, the deflection of a laser beam by the heat released in FMR has the potential to measure the local variation as well as the depth dependence of the magnetic permeability and that of the demagnetizing field. An experimental apparatus was described by Main and McCann [171] to detect EPR using a low-temperature version of the photoacoustic effect involving second sound in superfluid helium. The proposed technique works below 2 K and it is comparatively less sensitive to vibrational noise.

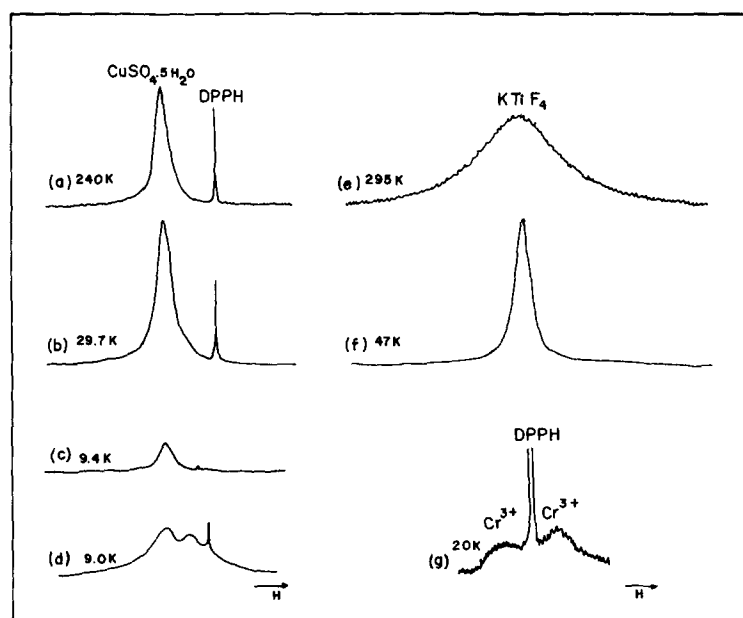


Fig. 20. Photoacoustically detected EPR spectra. (a), (b), (c), (d) $\text{CuSO}_4 \cdot 5\text{H}_2\text{O}$ and DPPH at different temperatures. Vertical amplification in (b) is that in (a) divided by 100. Comparison between (c) and (d) shows relaxation effects in the Cu^{2+} line. Spectrum (d) is recorded with a microwave power much larger than that used to obtain (c). (e), (f) KTiF_4 at 295 K and 47 K. Vertical amplification in (f) is that in (e) divided by 100. (g) Cr^{3+} lines in a ruby doped with magnesium (after Vasson and Vasson [160]).

5. Infrared photoacoustic spectroscopy

Most of the work done with photoacoustic spectroscopy (PAS) has been in the ultraviolet–visible region of the spectrum. This is primarily because the technique requires a moderately intense light source. As the photon energy decreases by two orders of magnitude and source brightness is diminished, there is a drastic decrease in the intensity of the PA effect in going from the visible to the IR range. Spectral features in this region can be directly related to molecular structure. The use of PAS in the near-IR region can be carried out using the same instrumentation as for the ultraviolet–visible region. The absorption bands observed in the near-infrared region for solid and liquid samples are mainly attributable to overtones and combinations of the fundamental vibrational modes of particular bonds; the most frequently observed bands are those relating to hydrogenic systems, e.g. $-\text{CH}$, $-\text{OH}$, and $-\text{NH}$.

The PAS applications in the near-IR have been well documented for analytical [172–175] and surface studies [172, 176, 177]. An interesting depth-profiling application of IR-PAS has recently been reported by Haas [178]. This author used the near-IR absorption of water, heavy water, and some primary alcohols (methanol, ethanol, propanol and butanol) to investigate their spectral changes as a function of the probing distance beneath the surface of the liquid–gas interface. This depth-profile analysis was carried out in the usual way, namely, by recording the PA spectra at different modulation frequencies. X-ray diffraction patterns suggest [178] that the structure of liquid alcohols (e.g. methanol) consists of similar chains of hydrogen-bonded molecules (polymer-like), in which each molecule is bonded to two other molecules; for water, the average number of nearest neighbors to any given molecule is 4.4. Water and alcohols show overtones and combinations due to stretching and bending vibrations of the O–H group. The alcohols also show this for the C–H groups. Furthermore, water and alcohols form associates by hydrogen-bonded hydroxyl groups. The formation of these associates influences the fundamental and overtone vibrations, and is reflected by the appearance of a diffuse absorption band of the hydrogen-bonded hydroxyls (polymer-like), slightly displaced towards longer wavelengths relative to the free (monomer) hydroxyl overtone.

In this work, Haas [178] reported on the spatial distribution of free and hydrogen-bonded hydroxyls in these liquids by recording the near-IR PA spectra at different modulation frequencies. In fig. 21 we show the PA signal of the first overtone of the hydroxyl vibration of methanol at three different modulation frequencies as obtained by Haas. A variation of the modulation frequency between 10 Hz and 2 kHz decreases the thermal diffusion length of the investigated liquids from about 60 μm (50 μm) to about 5 μm (4 μm) for water (methanol). The absorption band of the free hydroxyls (monomers) is located at 1394 nm, whereas the more diffuse absorption band of the hydrogen-bonded hydroxyls (polymers) is located at about 1550 nm. The latter band decreases considerably, relative to that of the monomers, with increasing modulation frequency, thereby entailing that an enhanced free monomer distribution with respect to the H-bonded distribution is expected as we move towards the liquid surface.

A similar IR depth-profile analysis was also reported by Ganzarolli et al. [179] for the case of solid low-density polyethylene. These authors have investigated the PA peak intensity ratios of the CH_3 , CH_2 , OH groups, relative to that of the methylene group, as a function of modulation frequency. The observed ratios increased as thinner, closer-to-surface polymers were sampled, which entails that closer-to-surface layers of solid polyethylene are richer in CH_3 , CH_2 , and OH groups than the bulk polymer.

A comparison between the PA and the Attenuated Total Reflectance (ATR) sampling depths in the

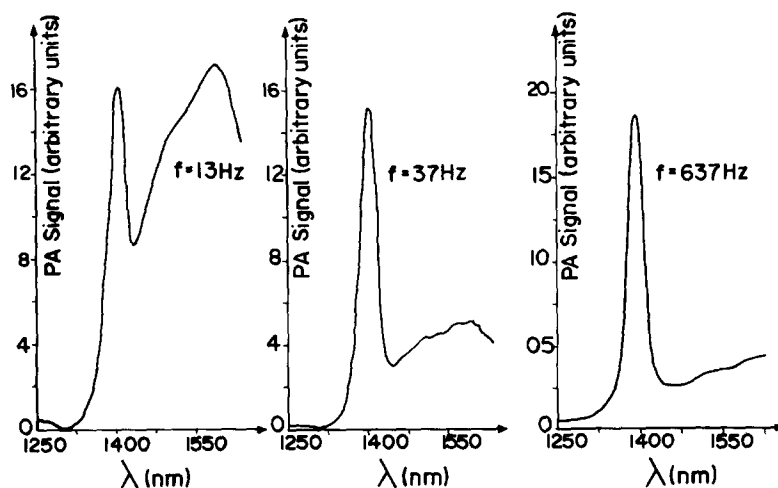


Fig. 21. The PA amplitude of the first overtone absorption band of the “free” and hydrogen-bonded hydroxyl vibration of methanol at three different modulation frequencies f of the incident light, as written on each diagram (after Haas [178]).

infrared region was further reported by Saucy et al. [180]. The maximum analytical depths of both techniques were compared using thin polymeric films. These films consisted of known thicknesses of polystyrene (PS) on poly(methylmethacrylate) (PMMA). The relative contributions of PS and PMMA to the spectra (at the 1601 cm^{-1} , 1732 cm^{-1} , and 3028 cm^{-1} bands) suggests that the maximum sampling depth of ATR is less than $2\text{ }\mu\text{m}$ while for PAS the maximum analytical depth extends to $15\text{--}20\text{ }\mu\text{m}$.

The use of PA detection in the infrared spectroscopy of opaque materials has also been the subject of considerable interest [181–190]. These studies are usually conducted using a Fourier Transform infrared spectrometer modified so that the sample chamber contains a PA cell. The use of Fourier Transform PAS was first introduced by Eyring and coworkers [189, 190] in the visible range. These authors have studied various samples like Nd-doped glasses, La_2O_3 , whole blood, etc. and showed that the use of Fourier Transform PAS considerably improves the signal-to-noise ratio due to the low brightness of lamp sources. In the IR region, the use of Fourier Transform PAS was first demonstrated by Rockley [181] by examining the PA spectra of polymer films and powdered samples. Other important advantages of using Fourier Transform IR PA spectroscopy (FTIR-PAS) over the conventional transmission or reflection spectroscopies were addressed by Royce and coworkers [191, 192] and by Viridine [182], especially when dealing with powdered samples. It regards the frequently observed spectral distortions of powdered samples dispersed on a transparent matrix due to light scattering. A decrease in the light scattering, when the refractive index of the matrix equals that of the powdered sample, causes an enhancement of the transmission (Christiansen effect). The use of FTIR-PAS eliminates this spurious effect as demonstrated by Royce and collaborators [191, 192] and Viridine [182]. Using a commercial FTIR spectrometer, Viridine [182] has clearly demonstrated the insensitiveness of the PA technique to the morphology of the sample, by preventing the problems with ungrindable samples, grinding artifacts, and light scattering, usually encountered in the pellet method.

Further aspects of FTIR-PAS have been discussed by several authors [188, 193]. In particular, Solomon and Carangelo [193] have made a comparative study of FTIR-PA spectra of Pittsburgh seam coal with those obtained from the KBr pellet and diffuse reflectance methods. In fig. 22a we show the KBr pellet, the PA and the diffuse reflectance spectra of the seam coal sample as obtained by Solomon and Carangelo [193]. A PA spectrum of improved quality using a sample cell developed at Ames

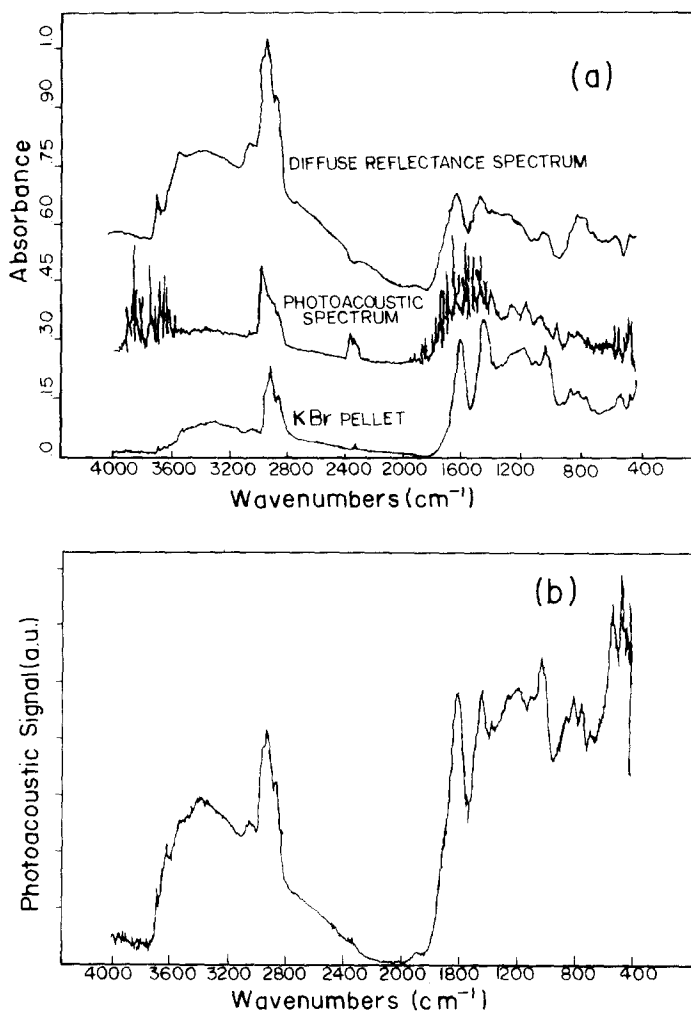


Fig. 22. (a) Comparison of FTIR spectra of Pittsburgh seam coal obtained by the diffuse reflectance, photoacoustic, and KBr pellet methods. (b) Photoacoustic spectrum of the same coal taken with a photoacoustic cell developed at the Ames Laboratory (after Solomon and Carangelo [193]).

Laboratory is shown in fig. 22b. These results clearly show the advantage of using FTIR-PAS over the more conventional techniques, when studying samples having low diffuse reflectance or properties incompatible with good contact with the ATR sampling surface. Additional examples of the use of FTIR-PAS in surface chemistry and catalysis studies can be found in refs. [194] and [195].

An interesting method for measuring large optical absorption coefficients with FTIR-PAS was recently proposed by Choquet et al. [196]. Without proper correction, FTIR-PAS can only lead to qualitative results unless the optical absorption coefficient is relatively small. By using the real and imaginary parts of the PA interferogram, these authors were able to simultaneously correct the frequency dependence of the PA signal, and the well-known PA signal saturation with increasing absorptivity. The method was experimentally tested with asbestos fiber samples.

Finally, we mention that, apart from gas-microphone detection, also PBD detection has been used in conjunction with a FTIR spectrometer [197-199]. The potentialities for IR studies of catalysis, corrosion, and other surface modification processes have been discussed by Palmer and Smith [197].

6. Thermal diffusivity measurements

The quantity which measures the rate of heat diffusion in the sample is the thermal diffusivity α . Apart from its own intrinsic importance, its determination gives the value of the thermal conductivity k , if the density ρ and the thermal capacity at constant pressure are known, since

$$\alpha = k/\rho c .$$

The importance of α as a physical parameter to be monitored is due to the fact that, like the optical absorption coefficient, it is unique for each material. This can be appreciated from the tabulated values of α presented by Touloukian et al. [200] for a wide range of materials, such as metals, minerals, foodstuffs, biological specimens and polymers. Furthermore, the thermal diffusivity is also known to be extremely dependent upon the effects of compositional and microstructural variables [201] as well as processing conditions, as in the cases of polymers [45, 202], glasses [203], metallic glass ribbons [207] and ceramics [201].

Thermal diffusivities of many materials can be accurately measured by the PA technique. This has been proved by several authors [45, 46, 202–210] and was first demonstrated by Adams and Kirkbright [205]. These authors have used the PA method to obtain the thermal diffusivity values for copper and glass by plotting the phase angle ϕ of the PA signal as a function of the square root of the chopping frequency ω . The basic idea of the method of Adams and Kirkbright can be understood by referring to the rear-illumination PA configuration schematically shown in fig. 23. The sample is periodically heated at its rear surface at $x = -l_s$, opposite to the sample–gas interface at $x = 0$. The resulting pressure fluctuation in the PA gas chamber can be calculated using the thermal diffusion model [14] outlined in section 2. Assuming that all the incident laser power is absorbed at $x = -l_s$, and neglecting the heat flux into the surrounding air, one obtains

$$\delta P = \frac{2P_0 I_0}{\sqrt{2} T_0 l_g a_g k_s \sigma_s} \frac{e^{j\omega t}}{(e^{l_s \sigma_s} - e^{-l_s \sigma_s})} , \quad (32)$$

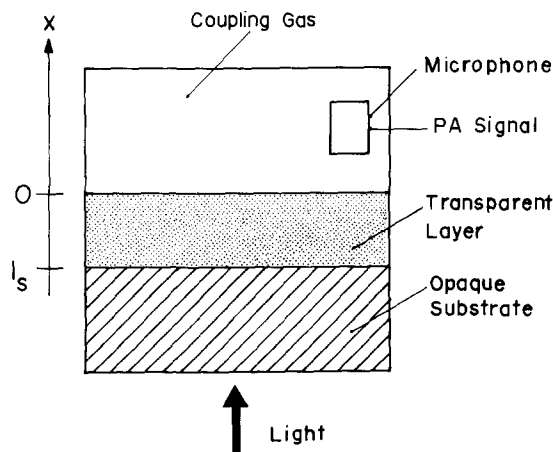


Fig. 23. Schematic rear-illumination PA configuration for measuring the thermal diffusivity as proposed in ref. [205].

where $\sigma_s = (1 + j)a_s$, $a_s = (\pi f/\alpha_s)^{1/2}$, and all the other symbols have the same meaning as in section 2. At high modulation frequencies, such that the sample is thermally thick (i.e., $l_s a_s \gg 1$), eq. (32) reduces to

$$\delta P = \frac{P_0 I_0}{T_0 l_g k_s a_s a_g} e^{-l_s a_s} e^{j(\omega t - l_s a_s)}. \quad (33)$$

The thermal diffusivity is obtained from the value of $l_s a_s = (\pi l^2 f/\alpha_s)^{1/2}$. This, in turn, can be obtained from eq. (33) either by a semilog plot of the PA amplitude versus \sqrt{f} or by a linear plot of the PA phase versus \sqrt{f} . Similar studies using data on the phase of the PA signal have been reported. For example, the thermal properties of polymer foils have been measured using this phase method by Merté et al. [202] and Lachaine and Poulet [210], whereas Kordecki et al. [204] and Swimm [209] have applied it to the thermal investigation of metallic glass ribbons and multilayer thin-film coatings, respectively.

Cesar et al. [207] adapted the Angström method [213] to photoacoustics by using the lateral heating configuration, shown schematically in fig. 24. It uses the optical transparency of the sample to a given wavelength for generating, through a lateral modulated illumination, a periodic heat source at a point x_0 of the sample. Performing the simple thermal diffusion calculations, these authors have shown that the pressure fluctuations in the gas chamber can be written as

$$\delta P = \text{const} \cdot e^{-\alpha_s x_0}. \quad (34)$$

Equation (34) entails that by measuring the PA signal, at a fixed modulation frequency, as a function of x_0 , the thermal diffusivity is readily obtained as the coefficient of x_0 in a semilog plot of the PA signal amplitude or a linear plot of the PA phase, as a function of x_0 . We note that even though this is a single modulation frequency method, the thermal diffusivity is also derived from an exponentially decreasing signal. Thus, the accuracy in the value of α_s is basically the same in these two methods. For a review on the PT determined thermal diffusivity in the case of semiconductors, we refer to the book of Mandelis [13], where further references can be found.

In order to improve the accuracy in the PT measurement of the thermal diffusivity, Pessoa et al. [212] have demonstrated the usefulness of a single modulation frequency PA method for measuring the

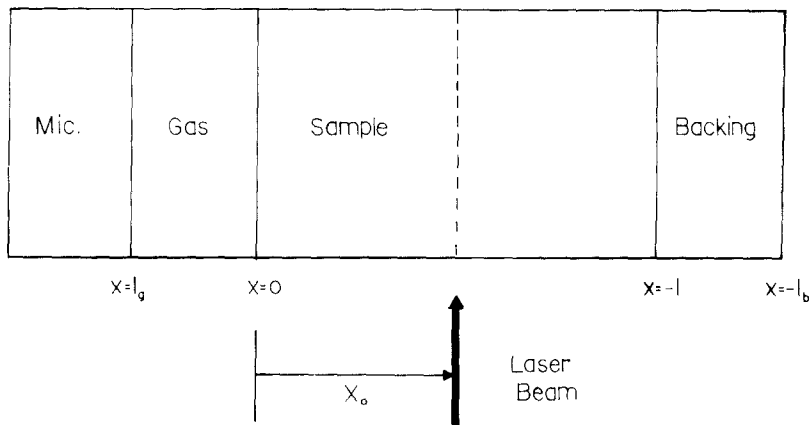


Fig. 24. Schematic lateral heating configuration for the PA measurement of the thermal diffusivity.

thermal diffusivity of solid samples. The method consists in measuring the relative phase lag $\Delta\phi = \phi_F - \phi_R$, at a single modulation frequency, between rear-surface illumination (R) and front-surface illumination (F). This method, called two-beam phase lag method, is an alternative to the one proposed by Yaza and Amer [208], in which the attenuation of the rear-illumination signal amplitude (S_R) relative to the front-illumination signal amplitude (S_F) is measured. In this latter case, as well as in most of the other conventional photoacoustic [202–211] and photothermal techniques [214], the thermal diffusivity is measured by recording the PA signal as a function of the modulation frequency. In contrast, in the two-beam phase-lag method the thermal diffusivity is obtained from a single chopping frequency measurement as follows. Using the thermal diffusion model of Rosencwaig and Gersho [14] for the production of the PA signal, the ratio S_F/S_R of the signal amplitudes and the phase lag $\Delta\phi$ for front- and rear-surface illumination (see fig. 25) are given by:

$$S_F/S_R = (I_F/I_R)[\cosh^2(la_s) - \sin^2(la_s)]^{1/2}, \quad (35)$$

$$\tan(\Delta\phi) = \tanh(la_s) \tan(la_s), \quad (36)$$

where I_F/I_R is the absorbed light intensity for front- (rear-) illumination. In arriving at eqs. (35) and (36) the authors [212] assumed that the sample is optically opaque to the incident light (i.e., all the incident light is absorbed at the surface) and that the heat flux into the surrounding air is negligible. In principle either eq. (35) or eq. (36) would give the value of α_s from a single modulation frequency measurement. However, since eq. (35) depends explicitly on the ratio I_F/I_R (i.e., one needs precise power monitoring and identical surface conditions on both sides of the sample), the value of the thermal diffusivity in the signal amplitude ratio measurement is obtained from the slope of the curve S_F/S_R as a function of the modulation frequency. In contrast, eq. (36) exhibits no explicit dependence on the absorbed power and surface conditions so that a single modulation frequency measurement is sufficient to derive the thermal diffusivity. Furthermore, the fact that the phase lag method is independent of power calibrations and surface conditions renders it a more precise technique than the amplitude ratio method.

The two-beam phase lag method has been applied to several samples ranging from optically opaque like semiconductors [212] to optically transparent like glasses [203] and polymer foils [45]. In table 3 we summarize the results obtained by Pessoa et al. [212] for several semiconducting samples using the two-beam phase lag method. The reproducibility of the method was checked at several modulation frequencies in the interval between 25 and 160 Hz. For these semiconductors the large optical

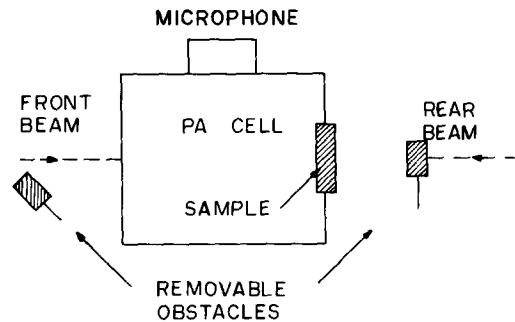


Fig. 25. Schematic arrangement for the two-beam photoacoustic measurement of the thermal diffusivity.

Table 3
Comparison of the thermal diffusivity values obtained from the two-beam phase lag method with the values quoted in the literature.

Material	Measured (cm ² /s)	Standard deviation	Literature values of α	Reference
Ge	0.35	0.01	0.346	200
Si	0.94	0.03	0.880	200
GaAs	0.24	0.01	0.21–0.26	200
GaSb	0.24	0.01	0.24	215
InP	0.45	0.02	0.46	215
InAs	0.22	0.01	0.19	215
PbTe	0.012	0.002	0.12	216

absorption in the visible region (i.e., $\beta > 10^4 \text{ cm}^{-1}$) ensures the condition of optical opaqueness implicit in eqs. (35) and (36). Figure 26 shows the dependence of the phase lag $\Delta\phi$ on la_s , as given by eq. (35). Also shown in fig. 26 are the experimental values for Ge and Si samples using the observed values given in table 3. The good agreement shown in fig. 26 between the theoretical predictions and the experimental data suggests that the proposed two-beam phase lag method may be used as a simple and accurate technique for thermal characterization of semiconductors. It also follows from fig. 26 that the method is valid for all values of la_s , i.e. for both thermally thick ($la_s \gg 1$) and thermally thin ($la_s \approx 1$) samples. In contrast, the method of Adams and Kirkbright [205] is valid only for the case of thermally thick samples, when the slope of $\Delta\phi$ as a function of la_s is one (i.e., the dashed line of fig. 26).

In the case of samples with large thermal expansion coefficients, such as polymers [45] and some glasses [203], the phase lag method is applicable only at low modulation frequencies. The reason for this is that the phase lag method, as outlined above, is valid only when thermal diffusion is the dominant mechanism responsible for the PA signal. When other effects, such as thermoelastic bending [44], come into play, the method is no longer straightforwardly applicable. This latter case occurs with samples having large thermal expansion coefficients. The failure of the phase lag method in these cases was

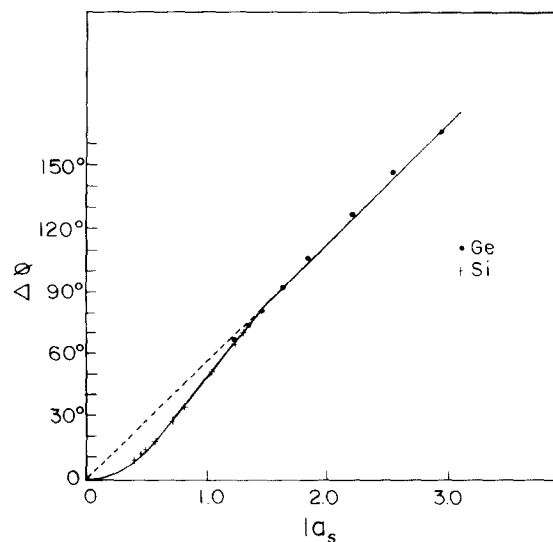


Fig. 26. Plot of $\Delta\phi$ versus la_s showing the experimental values for Ge and Si using the observed values of α . (After Pessoa et al. [212])

demonstrated in refs. [45] and [203]. In fig. 27 the semilog plot of the rear-signal amplitudes obtained by Leite et al. [45] for low-density polyethylene and teflon samples is shown as a function of the modulation frequency. In the 6–12 Hz frequency range, the rear-signal amplitude is dominated by an exponential behavior, $\sim \exp(-a\sqrt{f})$, as predicted by the thermal diffusion model, for a thermally thick sample. However, for frequencies greater than 15 Hz, the rear-signal amplitude behaves as f^{-1} , as shown by the solid curves in fig. 28.

This f^{-1} dependence for the rear-signal amplitude of a thermally thick sample means that thermal diffusion is no longer the dominant mechanism responsible for the PA signal. Leite et al. [45] have shown that the f^{-1} frequency dependence is what is expected for the behavior of the PA signal amplitude when we take into account the contribution from thermoelastic bending. These authors then concluded that, in the frequency range where thermoelastic bending is dominant, the thermal diffusivity is no longer obtained from the front- and rear-phase difference but rather from the modulation frequency dependence of either recorded phase. In fact, it was shown in ref. [45] that the frequency dependence of the front-phase signal is given by

$$\phi_F = -\pi/2 + \arctan(1/z - 1), \tag{37}$$

where $z = l_s a_s$. Using eq. (37) in the high-frequency range ($f > 15$ Hz), these authors have deduced the values of α for the polymer foils studied. This is summarized in table 4, where the good agreement between the two methods can be seen.

In addition to the gas–microphone PA technique several other PT techniques have been developed for measuring the thermal diffusivity. These include PBD [218], the converging thermal wave technique [219], correlation PA spectroscopy [220], and pyroelectric detection [104, 108]. An improved gas–microphone detection technique especially suitable for measuring the thermal diffusivity has recently

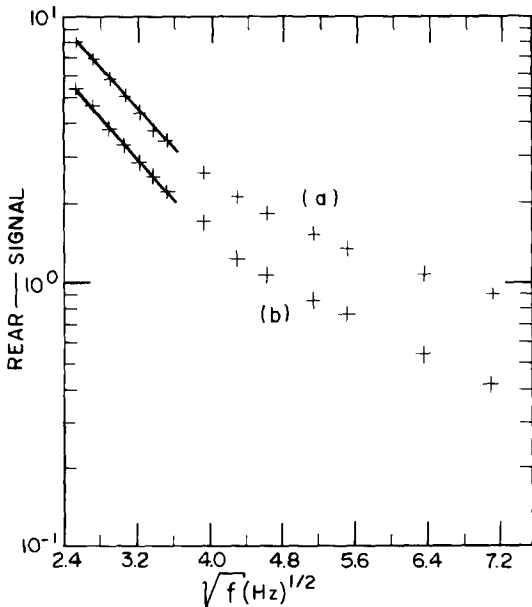


Fig. 27. Semilog plot of the rear-signal amplitude versus \sqrt{f} for (a) LDPE and (b) PTFE (after Leite et al. [45]).

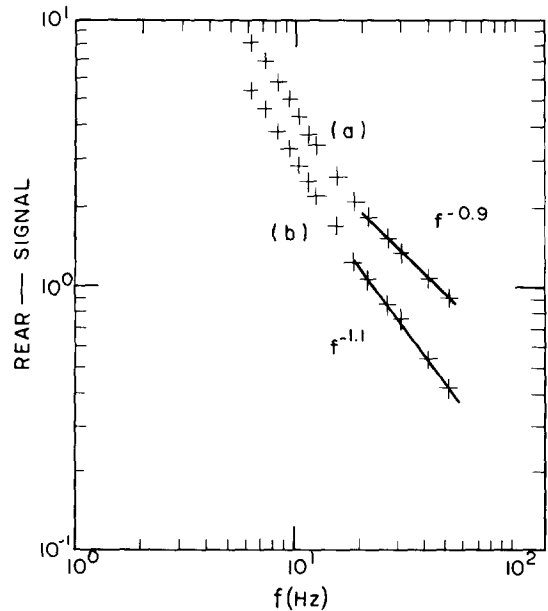


Fig. 28. Log–log plot of the rear-signal amplitude versus the modulation frequency f for (a) LDPE and (b) PTFE (after Leite et al. [45]).

Table 4
Thermal diffusivity values obtained from a fit of the front-phase data using eq. (37) of the text. The literature values were taken from ref. [217].

Material	Front-phase data fit (cm ² /s)	Literature values (cm ² /s)
Teflon	0.0014	0.0011
PVC	0.0006	0.0008
Cellulose acetate	0.0008	0.0009
Polypropylene	0.0007	0.0008
Low-density polyethylene	0.0016	0.0016

been proposed by Ferreira et al. [221]. It is based on the use of an open photoacoustic cell discussed in section 2 (cf. fig. 7). These authors have used this minimal-volume gas–microphone detection technique for measuring the thermal diffusivity of $\text{Pb}_{1-x}\text{Sn}_x\text{Te}$ alloys as a function of the Sn content. This open-cell configuration is an attractive and simple technique presenting some advantages over conventional closed-cell detection. The use of a minimal gas chamber ensures an enhanced signal-to-noise ratio, and, consequently, higher accuracy in the value of α , and offers greater adaptability to practical restrictions imposed by experimental system requirements, especially when minimal preparation is required. The simplicity and accuracy of the different photothermal techniques outlined above may render them as a standard thermal characterization method.

7. Investigation of phase transitions

The PA technique, besides providing us with the value of the conductivity k (if the diffusivity α is known), allows us to study changes in the thermal parameters as the experimental conditions change. Florian et al. [222] were the first to report such a study. They investigated the first-order liquid–solid transition in Ga at 303 K and in water at 273 K and the structural phase transition in K_2SnCl_5 at 263 K. Even for transparent materials, the PA detection of phase transitions is still possible. This is done through the aid of small carbon particles in intimate thermal contact with the material under study.

The possibility of using the PA effect for the study of the thermal conductivity and the specific heat was demonstrated by Siqueira et al. [223] by studying the temperature dependence of the PA signal of polycrystalline Al-doped VO_2 . These authors and Fernandez et al. [224] have pointed out that the PA method can yield quantitative information about the product of the temperature dependent thermal conductivity and the specific heat of a solid sample using the RG theory, provided the thermal response of the PA cell is known and normalized in the entire temperature range of the experiment.

In fig. 29 we present the PA signal dependence on the temperature for the Al-doped VO_2 sample as reported by Siqueira et al. This curve suggests the existence of a second-order phase transition with a transition temperature around 47°C. In fig. 30 the normalized product of the temperature dependent thermal conductivity and the temperature dependent specific heat is shown. The curve was generated from the inverse of the PA signal. The data have been normalized by the cell response function. The jump in fig. 30 between 308 K and 338 K was attributed to the jump of the specific heat, thus defining a phase transition at $T_n = 47 + 273 = 320$ K. This value of T_n agrees very well with the NMR result and corresponds to the transition from the M_0 phase to the mixed $M_1 + M_2$ phase of Al-doped VO_2 . Other

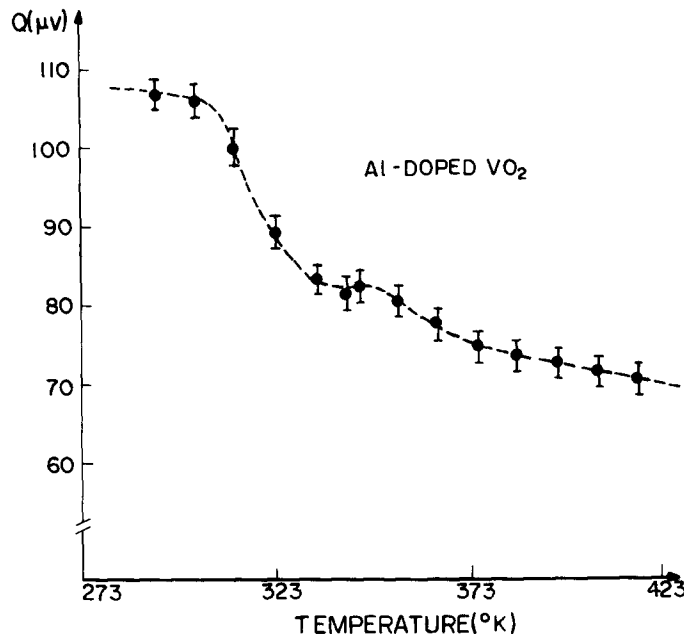


Fig. 29. Photoacoustic signal Q of 0.8 at% Al-doped VO_2 as a function of temperature (after Siqueira et al. [223]).

phase transitions can be observed according to the authors: one between 343 and 363 K, probably due to the transformation from the $M_1 + M_2$ to the M_2 phase, and another one, between 363 and 373 K, due to the transformation from the M_2 phase to the metallic phase. In the calculation of the curve $c_s(T)k_s(T)$ as a function of the temperature the thermal conductivity $k_s(T)$ was assumed to be a smooth function of the temperature.

Previously, Pichon et al. [225], using the RG theory, have demonstrated that in the case of thermally

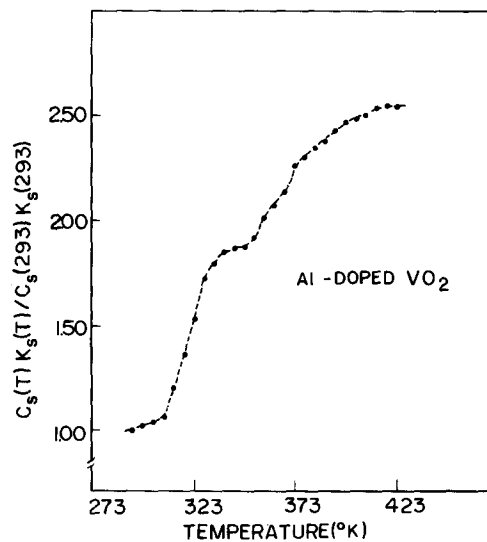


Fig. 30. Temperature variation of $c_s(T)k_s(T)$ of Al-doped VO_2 normalized by the cell response function (after Siqueira et al. [223]).

thick samples, whose thermal diffusion length is smaller than the optical absorption length, the PA signal is proportional to $(\mu_g/T_0)(2/\omega_s c_s)$, where the quantity μ_g/T_0 is a well-known slowly varying function of the temperature [225]. These authors have used this expected c_s^{-1} dependence to observe the specific heat anomaly of various antiferromagnetic dielectric samples close to the Néel temperature, as, for example, in the case of crystalline CrCl_3 and MnF_2 . Figure 31 shows the deduced temperature dependence of c_s in MnF_2 around 68 K. As we can see, their theoretical prediction is in reasonable agreement with experimental photoacoustic data. The anomaly is comparable to that observed using conventional calorimetric measurements. Korpiun and coworkers [226–230] have performed extensive experimental and theoretical investigations in this area. A theoretical model [226] for the PA amplitude and phase angle at a first-order phase transition was generalized [230] to arbitrary thermal thickness of the sample. The results of their measurements at the melting point of indium and at the glass transition region of polystyrene confirmed their model [230].

A detailed investigation of the PA detection of phase transitions has been reported by Pelzl and coworkers [231]. These authors have investigated the interplay between the thermoacoustic and the thermoelastic effects in the PA detection of phase transitions. Near phase transitions the relative contributions of both mechanisms change markedly, thereby providing a sensitive tool for the study of thermal properties in the vicinity of a transition point. Their measurements were performed on thin Gd disks near the magnetic ordering temperature of this rare-earth metal at about 292 K. Their results were analysed on the basis of the composite piston model described in section 2. The cell design they used is similar to the one used in the phase lag method described in section 6 (cf. fig. 25). This design allows for both rear- and front-illumination configurations. The cell is mounted into a cryostat where the temperature of the whole assembly can be slowly and continuously changed. In fig. 32 we show the temperature dependence of the front-illumination PA signal phase angle of a $110 \mu\text{m}$ thick Gd disk at different chopping frequencies. At low frequencies the PA signal essentially reproduces the temperature variation of the specific heat; with increasing modulation frequency, the thermoelastic motion of the disk starts to dominate the change of the signal at the transition point. The good agreement between

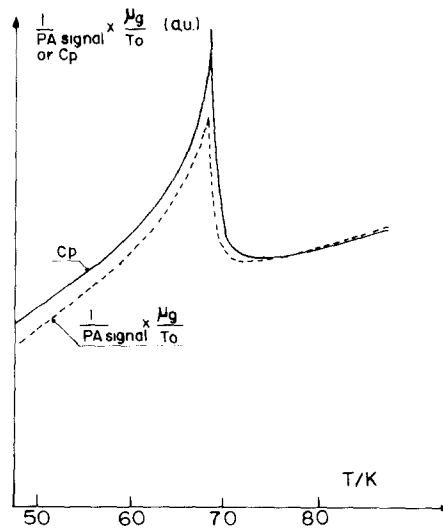


Fig. 31. $(1/\text{PA signal})(\mu_g/T_0)$ of an MnF_2 sample versus temperature (dashed line) and c_p value versus temperature obtained by conventional calorimetric measurements (after Pichon et al. [225]).

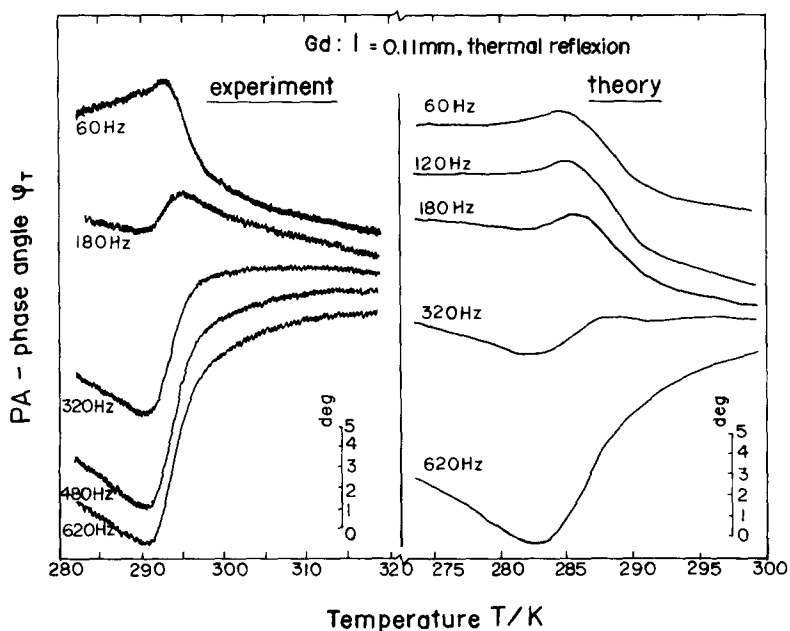


Fig. 32. Temperature dependence of the PA phase angle recorded from a Gd foil with a thickness of 0.11 mm: experiment (left) and theory (right) (after Junge et al. [231]).

their theoretical predictions and their experimental results was then argued by the authors to be in favor of their proposed method for determining both the specific heat and the thermal expansion coefficient near the transition point.

The PA detection of phase transitions has also been reported by other authors both at low [232–234] and high [235–237] temperatures. In particular, Bechthold et al. [237] have suggested a photoacoustic cell design appropriate for the 300–1050 K temperature range and used it to study both first- and second-order phase transitions in metal–hydrogen alloys (e.g., NbH_x , TaH_x , and VH_x). In this work, Bechthold et al. [237] pointed to the possibility of using the method to study phase diagrams and to gain information on the thermal parameters of the materials involved.

In a subsequent work, Bechthold and Campagna [234] described a new low-temperature photoacoustic cell, which allows continuous variation of the temperature between 90 K and 320 K. To demonstrate the applicability of such a cell, the temperature dependence of the electronic ground state of solid Fe(III) diethyldithiocarbamate was investigated for the first time spectroscopically in the visible and ultraviolet spectral range. These authors also reported for the first time the PA detection of excitonic states in semiconductors, which allows the non-radiative decay in epitaxial layers to be directly studied. This is shown in fig. 33, in which the PA signal at 90 K of two excitons in an epitaxially grown film of nitrogen- and tellurium-doped GaP on a GaP substrate is depicted. Both the amplitude and phase of the spectra are shown. The peak observed at 536.9 nm corresponds to the exciton bound to the isoelectronic nitrogen impurity. The second weaker line observed at 538.7 nm was assigned by the authors to the tellurium exciton. The Te exciton can be better identified in the phase spectra than in the amplitude spectrum as shown in fig. 33.

The investigation of phase transitions has also been carried out using other photothermal detection techniques. Mandelis et al. [238] have recently reported on the use of the PP technique to study the thermal property changes of solid samples near transition points. To demonstrate the usefulness of this

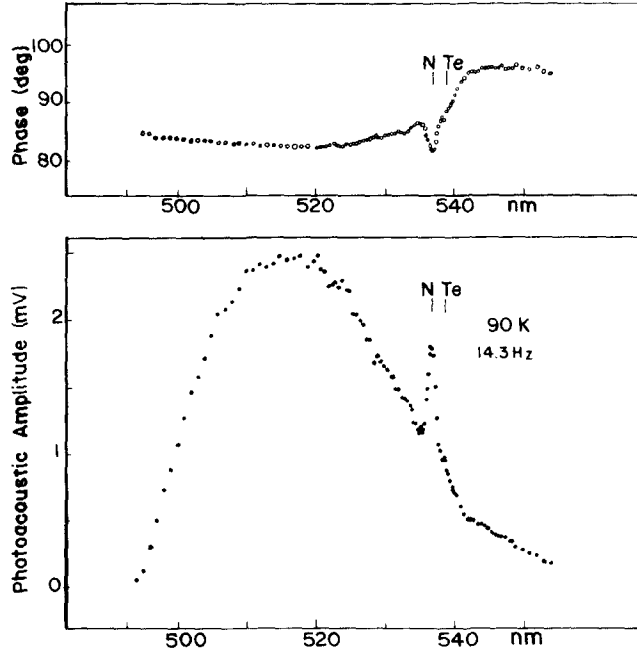


Fig. 33. Photoacoustic detection at 90 K of nitrogen- and tellurium-bound excitons in an epitaxial GaP layer on GaP (after Bechthold and Campagna [234]).

technique to specific heat data acquisition around the transition temperature, these authors have applied this technique to powdered samples (e.g., Rochelle salt and Al-doped VO_2) exhibiting first- and second-order transitions. Both theoretical and experimental results indicate the capability of the PP technique to measure specific heat profiles, using very simple experimental apparatus compared to gas-microphone detection.

8. Deexcitation processes

The PA effect is selectively sensitive only to the heat-producing deexcitation processes that take place in the sample after the absorption of modulated light. In general, apart from the thermal deexcitation channel, several other deexcitation channels, such as fluorescence, photochemistry, photoconductivity, etc., are simultaneously competing with each other. Denoting by E_0 the energy absorbed by a given system, the heat produced can be expressed as

$$Q = E_0 \left(1 - \sum_i \gamma_i \right), \quad (38)$$

where the γ_i are the conversion efficiencies of the several non-thermal deexcitation channels. Since the PA signal is proportional to Q , it can, in general, be written as

$$S = S_0 \left(1 - \sum_i \gamma_i \right), \quad (39)$$

where S_0 represents the PA signal if only the thermal deexcitation channel is active. Equation (39) tells us that the PA signal is complementary to the other photoinduced energy conversion processes. That is, when an optically excited energy level of a given system decays by means, say, of fluorescence or undergoes a photochemical reaction, then little or no acoustic signal is produced.

This complementary aspect of the PT signal has been explored by several authors for investigating photoinduced conversion processes, ranging from fluorescence studies in solids and liquids to photochemical reactions and the photovoltaic effect in semiconductors. The first experiment showing the sensitivity of the PA effect to fluorescence was reported by Rosencwaig [239] by comparing the gas-microphone detected signals of Co- and F-doped Ho_2O_3 and pure Ho_2O_3 powders. The fluorescence of pure Ho_2O_3 is strongly quenched in the presence of the Co and F impurities, so that both the fluorescent and non-fluorescent lines of doped Ho_2O_3 appear in the PA spectrum. In the case of pure Ho_2O_3 the fluorescent levels have their intensity in the PA spectrum greatly reduced, since these levels are now deexciting through the emission of photons rather than through heating the sample.

Following this pioneering paper of Rosencwaig, it was soon realized that the PA technique could be used to measure quantum efficiencies of fluorescent states. These studies were carried out initially by Lahmann et al. [50] and by Starobogatov [240] using PZT detection, and by Adams et al. [241] using gas-microphone detection. The samples studied by these authors were dye solutions, and the method employed consisted in comparing the PA signals from these dyes with the ones from appropriate non-fluorescent solutions. The measured quantum yields agreed with those obtained by conventional luminescence experiments, and the accuracy appeared to be better. In the case of solid samples, the first quantum efficiency experiments were reported by Murphy and Aamodt [242] for $\text{Cr}^{3+}:\text{Al}_2\text{O}_3$ samples, by Merkle and Powell [243] for $\text{Eu}^{2+}:\text{KCl}$ samples, and by Quimby and Yen [244] for Nd^{3+} ions in an ED-2 glass matrix.

In the case of photochemical studies the first report on the PA monitoring of a photochemical reaction was given by Rosencwaig [239] using gas-microphone detection. The sample used was a photosensitive material, namely, copper blue. This compound is colorless in the dark, but turns strong blue when exposed to short wavelength light. By recording the PA spectrum of copper blue at different times, Rosencwaig was able to monitor the time evolution of the two characteristic strong absorption bands around 400 and 600 nm responsible for its blue color. These bands arise from a photochemical change in copper blue wherein some of the photons absorbed at short wavelengths are used to break a ring in the copper blue molecule, thus creating a new compound.

Other photochemical reaction PA studies in biological samples as well as on photodissociation of molecules [245], and on photochemical gas generation and consumption [246] have also been reported.

In the case of materials with large photovoltaic effect (conversion of the light energy into electrical energy) the deexcitation complementary aspect of the PA signal can be used to monitor the photovoltaic conversion efficiency. Cahen [247] was the first to demonstrate this possibility, using a Si solar cell. In a photovoltaic device, the photovoltaic conversion efficiency $\gamma(R_L)$ is a function of the external electrical load R_L . If the photovoltaic deexcitation process is the dominant deexcitation process, as in silicon, eq. (39) can be written, for a specific load resistance R_L , as

$$S(R_L) = S_0[1 - \gamma(R_L)], \quad (40)$$

where S_0 is a constant for fixed cell geometry, modulation frequency, optical wavelength, and incident light intensity. Under open-circuit (OC) conditions, the photovoltaic device has zero energy conversion efficiency, i.e., $\gamma = 0$, and one has

$$S(OC) = S_0 . \quad (41)$$

Combining eqs. (40) and (41), one gets

$$\gamma(R_L) = 1 - S(R_L)/S(OC) . \quad (42)$$

This result tells us that the photovoltaic conversion efficiency can, in principle, be readily measured as a function of the light wavelength, as well as of load resistance, using the PA effect. Figure 34 shows Cahen's results for a Si solar cell using gas-microphone detection. In fig. 34 both the PA signal amplitude and the measured electrical power are shown as a function of the load resistance. As expected from eq. (42), the PA signal exhibits a minimum when the output electrical power is at a maximum. From this minimum, a maximum conversion efficiency of about 17.5% is obtained at an optimum load resistance of roughly 6Ω , for the wavelength used. Since this pioneering work of Cahen, and despite the fact that a variety of PT detection techniques have been successfully developed in the last decade, only recently the use of these PT techniques has been reported for measuring the photovoltaic conversion efficiency of solar cells. These include the PTR [248], the PP [111], and the PBD [249] techniques. A detailed study of the photovoltaic characterization of solar cells using the PA signal phase of gas-microphone detection was reported by Cahen and Halle [250].

The simplicity of Cahen's [247] experiment suggests an important application of the PT technique in testing and quality control of solar cells. However, the recent PTR [248] and PP [111] experiments on the photovoltaic conversion efficiency measurements using these two distinct PT detection techniques have demonstrated that some caution should be exercised when applying the PT signal to get an absolute measurement of $\gamma(R_L)$. The point raised in these papers, and further demonstrated by Mello

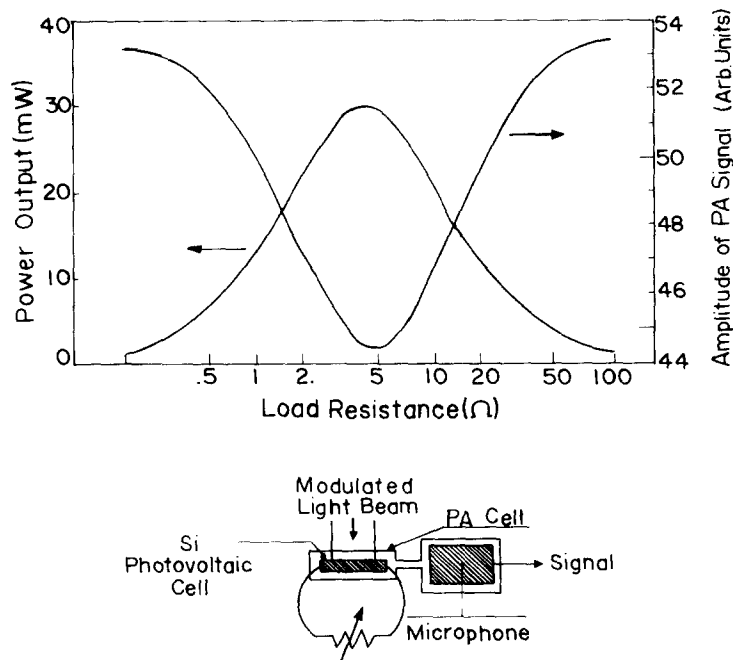


Fig. 34. PA monitoring of the photovoltaic effect in a solar cell (after Cahen [247]).

et al. [251] and Riette et al. [249], is that eq. (40) can be regarded as a good prescription for obtaining $\gamma(R_L)$ only if all the other contribution channels (such as luminescence, Joule heating of carriers, photochemical, etc.) are negligible. In particular, as shown in refs. [248] and [111], depending on the detection technique used, the Joule heating gives a dominant contribution especially at small values of the external load resistance, thereby affecting the value of the optimum conversion efficiency.

Figure 35 shows the results for $\gamma(R_L)$ for a p-n solar cell illuminated at 18 Hz by a 5.2 mW He-Ne laser, using both the PP and the PA techniques, as given by Faria et al. [111]. The PA data were obtained using conventional gas-microphone detection with the back contact of the Si cell flushed against the back wall of the PA chamber. The PP data were recorded using a thin pyroelectric film (e.g. PVF_2) in intimate contact with the (non-illuminated) back surface of the solar cell. Both curves in fig. 35 show a clear maximum around the optimal load resistance R_L^* . The PA-determined optimal load resistance, $R_L^*(\text{PA}) = 350 \Omega$, agrees quite well with that determined from electrical measurements, whereas the PP-determined optimal load resistance, $R_L^*(\text{PP}) = 400 \Omega$, is slightly higher. Two other significant differences between the PA and PP conversion efficiencies can be noted. First, the value of γ at the optimal load resistance obtained from the PA measurement is about 12%, while the correspond-

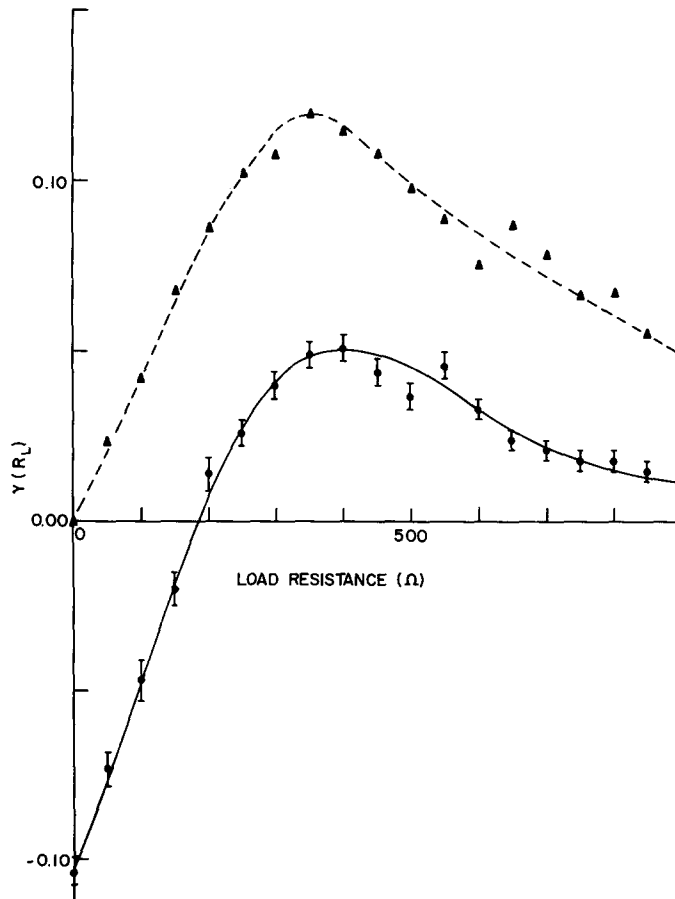


Fig. 35. Photopyroelectric γ_{PP} and photoacoustic γ_{PA} (dashed) conversion efficiencies as a function of the load resistance R_L , for a 500 μm thick p-n solar cell, at 18 Hz under ~ 5.2 mW He-Ne laser illumination. At 350 Ω the PA-determined conversion efficiency is $\sim 12\%$, whereas the PP-determined optimal conversion efficiency is $\sim 5\%$ at 400 Ω . (After Faria et al. [111])

ing PP value is about 5%. Second, the PP-determined γ , as given by eq. (42), becomes negative for $R_L < 200 \Omega$. This latter feature suggests that the pyroelectric measurement is sensitive to some additional heat sources resulting from the illumination.

To explain these differences between the PA and PP conversion efficiencies, Faria et al. [111] resorted to the simple model for a p-n junction-type solar cell shown in fig. 36. The radiation absorbed within one carrier diffusion length from the junction generates a current I_{SC} and a voltage V_J . This current splits into two components, one, I_L , which flows through the diode to the load, and another one, I_J , which is injected across the junction. The additional heating sensed by the PP measurement was attributed by Faria et al. [111] to the current dissipation at the internal resistance R_S , given by $Q_S = R_S I_L^2$. This possible explanation was checked by measuring the PP signal at 200 Hz. At this frequency the sample is thermally thick so that the PP signal dependence on R_L would eventually single out the additional heating mechanism. Figure 37a shows the dependence of the normalized PP signal, $S(R_L)/S(OC)$, as a function of R_L , while in fig. 37b the dependence of I_L^2 on R_L is plotted. The remarkable similarity between these two plots suggests that the additional heating is, indeed, provided by the dissipation of I_L through R_S .

This Joule heating is mainly generated in the base region of the solar cell and could, in principle, also contribute to the PA signal. The PA measurements, both at low and high modulation frequencies, showed, however, that this additional heating is strongly damped so that the PA detection senses mainly the front surface contribution, as suggested by Cahen and Halle [250]. Faria et al. [111] attributed this to a preferential heat flow towards the silvered back contact of the solar cell for the heat generated in the base region. The thermal conductance to the silvered back contact is roughly three times larger than that towards the Si, so that the back contact may be viewed as a heat sink. Since in the PP technique this heat sink is in intimate thermal contact with the pyroelectric film, it is not surprising that the PP signal senses the Joule heating. In the PA case, this heat reaching the back contact is dissipated through the PA cell walls so that only the front surface contribution is detected.

This explanation was further checked with gas-microphone detection in a PA transmission configuration; Mello et al. [251] have used conventional PA detection in which they have reversed the sample positioning in the PA chamber such that the silvered back contact of the solar cell was facing the gas

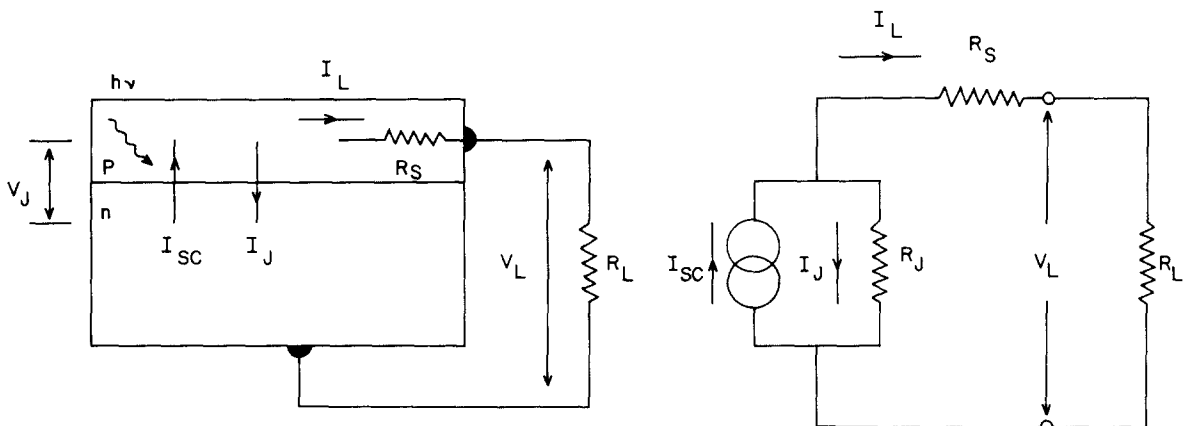


Fig. 36. Equivalent circuit of a p-n solar cell. R_L is the load resistance, R_S is the internal series resistance of the diode including the contact resistance, R_J is the junction resistance, I_{SC} is the short circuit current, I_J is the current injected across the junction, and I_L is the load current. The internal resistance R_S was found to be equal to 6.5Ω as determined from the dark-current characteristics of the junction. (After Faria et al. [111])

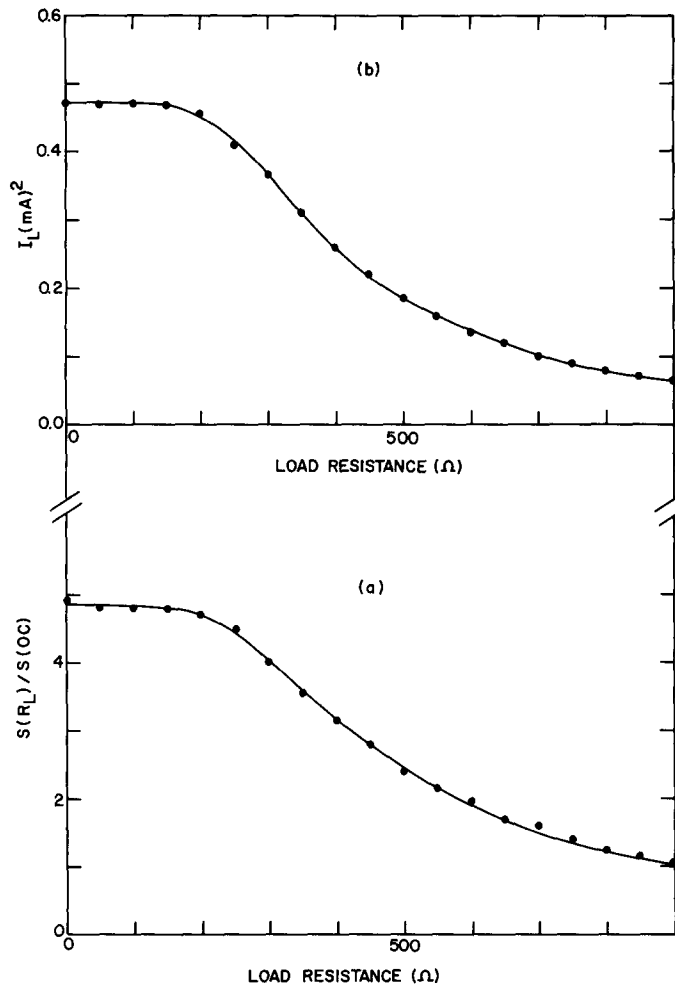


Fig. 37. (a) PP signal for the solar cell, as a function of the load resistance at 200 Hz under ~ 5.2 mW He-Ne laser illumination. (b) Dependence of the square of the load current I_L (mA) on R_L , as obtained from electrical measurements (after Faria et al. [111]).

inside the PA cell. In this case the PA detected signal also exhibited the Joule heating contribution as in the PP detection. We refer the reader to refs. [248–251], where a more detailed discussion can be found.

Thielemann and coworkers [252, 253] have applied gas-microphone detection to determine the photogeneration quantum efficiency of Schottky diodes.

Another important class of problems that have been studied using the PT detection techniques is that of monitoring transport properties and non-radiative processes in semiconductors. This subject has recently been reviewed in ref. [214]. The influence of transport properties (e.g. carrier lifetime, carrier diffusion length, surface recombination velocity, etc.) and non-radiative states on the PT signal of semiconductors may be physically seen as follows. The absorption of light generates a distribution of excess carriers in the sample. These excess carriers diffuse through the sample and reestablish equilibrium by disposing of the energy in excess both by emitting radiation and by generation of heat.

The heat generation during this process of reestablishment of equilibrium is essentially due to intraband transitions in the bulk, non-radiative band-to-band transitions, and non-radiative surface recombinations generated within a diffusion length from the surface. Apart from this, the PT effect in semiconductors is also sensitive to the presence of non-radiative states near the surface of the sample.

Spectroscopic examples of the influence of the finite carrier lifetime and diffusion coefficient as well as of non-radiative transitions in the PA signal were first given by Ghizoni and coworkers [254] and by Mikoshiba et al. [255] in the case of PZT detection. Following the work of Bandeira et al. [254] several authors [256–260] have extended their model to include the effect of surface band bending [255, 258] as well as of an alternating electric field [259, 260]. The influence on the PA spectrum of non-radiative states, due to native defects near the band gap of CdS, Si, GaAs and InP has been discussed by Wasa et al. [261, 262]. Apart from the gas–microphone and the PZT detections, Amer and coworkers [263] have recently proposed a spatially resolved technique, based upon PBD detection, for investigating the transport properties of semiconductors. Using this PBD detection, these authors were able to obtain in situ information on the transport properties anywhere within or at the surface of p-type Si samples with different surface treatments.

Finally, thermal wave detection has also been applied to non-spectroscopic studies of transport phenomena in semiconductors, such as acoustic wave instabilities. The earliest experiment on the PA detected acoustic wave instability in semiconductors was reported by Ghizoni et al. [264]. In this experiment, the periodic heating of a Si sample due to the electron drift in an electric field was studied. Under a d.c. electric field, the free carriers of a semiconductor, gaining energy from the field, ultimately establish a steady state where the energy gained from the field equals the energy lost to the lattice via the electron–photon interaction. Hence, by pulsing a d.c. voltage in a semiconductor, mounted in a PA cell as shown in fig. 38, this periodic heating can be detected by the microphone. Figure 39 shows the acoustic signal of a Si sample as a function of the pulse amplitude V_p for two different sample thicknesses and different values of the pulse duration τ_p . Figure 40 shows the variation of the detected acoustic signal as a function of the pulse duration. These data indicate that at low values of the electric field $E = V_p/d$, the acoustic signal S is simply given by the Joule heating, that is, $S \sim E^2$. However, at high fields, the signal increases exponentially, such that $S \sim \exp(E\tau_p)$.

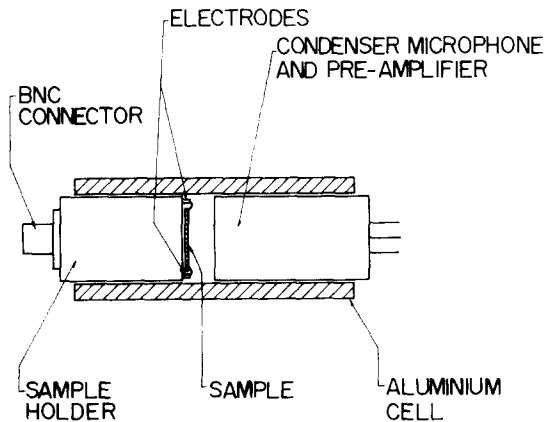


Fig. 38. Acoustic cell used for investigating the transport properties in semiconductors (after Ghizoni et al. [264]).

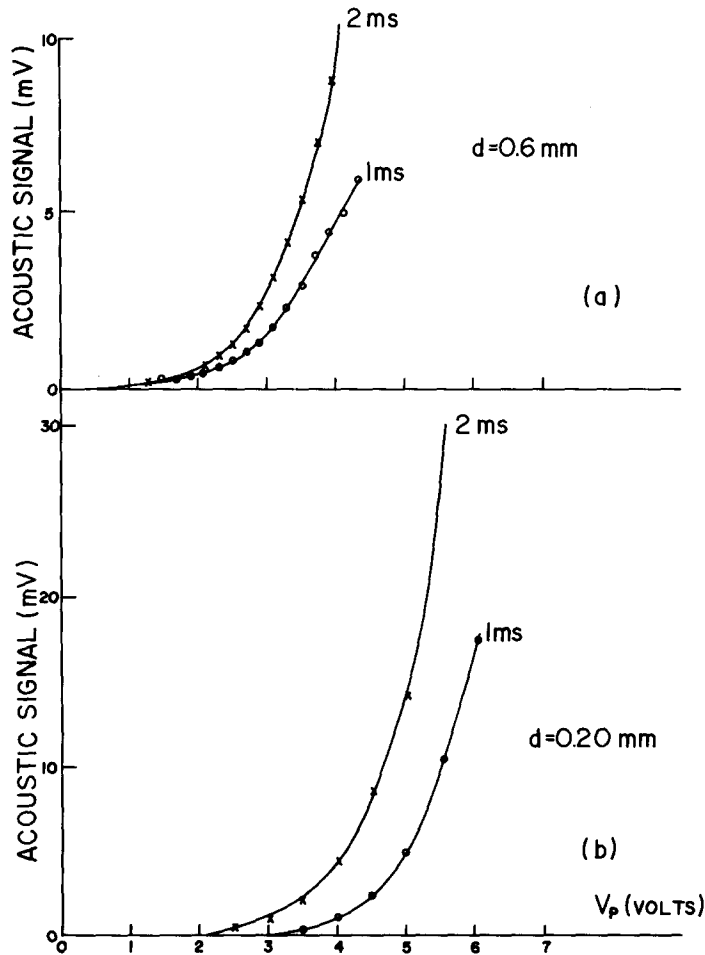


Fig. 39. Acoustic signal versus the applied peak voltage (V_p) for various pulse durations (τ_p). Sample thickness (a) $d = 0.6$ mm; (b) $d = 0.2$ mm. (After Ghizoni et al. [264])

These results were explained by Ghizoni et al. [264] as a result of the onset of the acoustoelectric instability in the sample. As is well known [265], in the presence of drifting carriers, the phonon relaxation time gets negative (i.e., one has amplification) when the drift velocity V_d exceeds the sound velocity. Under such conditions, phonon-stimulated emission dominates over the phonon relaxation and the acoustic signal grows exponentially; i.e., for fields greater than the threshold field, given by $\mu E = V_s$, there is a phonon gain in the medium as manifested by the exponential growth of the signal shown in figs. 39 and 40.

More recently, Rodrigues et al. [267, 268] have used pyroelectric detection to investigate the acoustic wave instability in Ni due to a temperature gradient (i.e. the so-called thermoelectric amplification of acoustic waves [266]). The temperature gradient was established by means of 100 ns CO_2 laser pulses focused on the Ni sample. The detection system consisted of a $28 \mu\text{m}$ thick PVF_2 film in intimate contact with the sample. The value for the critical laser fluence required to observe the exponential growth of the PT signal agreed quite well with the one predicted by the theory.

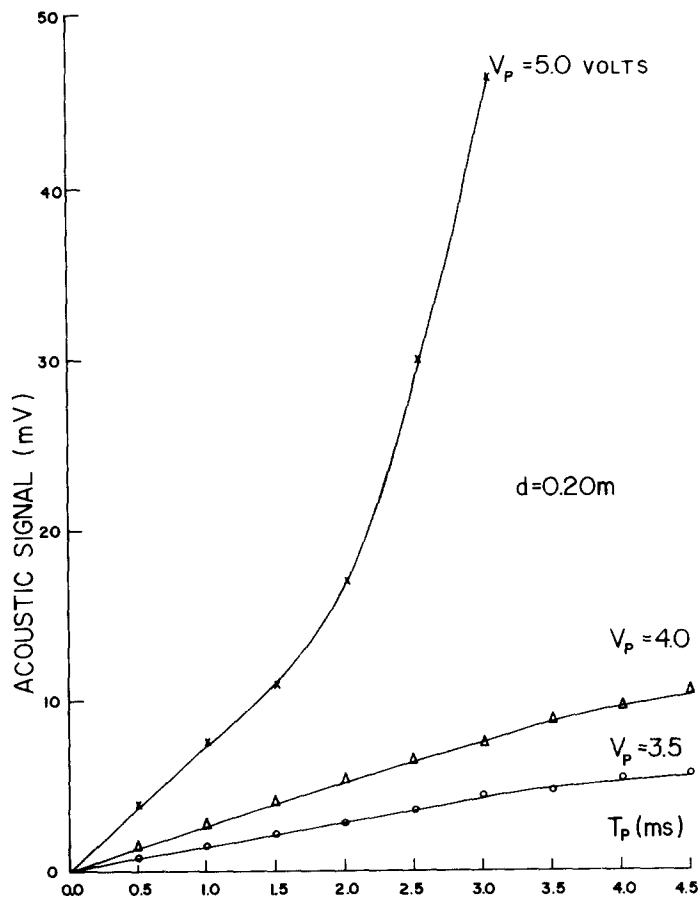


Fig. 40. Acoustic signal versus pulse duration for different values of the amplitude V_p (after Ghizoni et al. [264]).

9. Biological applications

Biological and medical applications of the PA technique have been described elsewhere [269–273]. In many cases PAS is an alternative method for studying biological materials not suitable for conventional spectroscopic techniques such as transmission or reflectance, due to scattering properties. In the following we give some typical examples of these applications. In particular, we will choose examples predominantly from the most recent literature, i.e. from 1980 onwards, since earlier reviews have covered the period before 1980. The capability of PAS for obtaining biological spectra of samples of different types has been first illustrated by Rosenzweig [3]. The PAS spectrum of a smear of whole blood shown in fig. 41 exhibits the characteristic spectrum of oxyhemoglobin as clearly as in the PAS spectrum of red blood cells and even of the extracted hemoglobin itself. Thus, it is possible to monitor the optical properties of hemoglobin directly in the blood with minimal interference of highly scattering non-absorbing components in blood cells. That is, in situ, without resort to an extraction procedure. Being a non-invasive technique PAS is particularly suitable for condensed phase samples. Balasubramanian et al. [274] used this technique to monitor the malaria parasite in order to establish the nature of this pigment, provide direct evidence of drug interactions in the parasite, and distinguish drug-sensitive strains of resistant microorganisms.

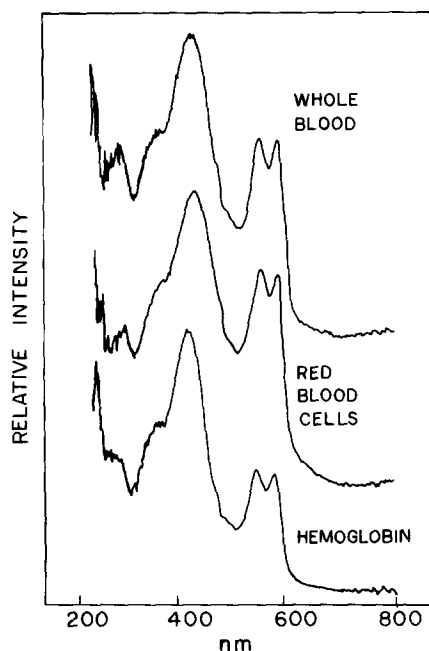


Fig. 41. Photoacoustic spectra of smears of whole blood, red blood cells, and hemoglobin. All three spectra clearly show the band structure of oxyhemoglobin. (After Rosenzweig [3])

For a multicomponent or layered system, an important question that has attracted the attention of a number of workers in PAS regards its unique capability of resolving the spectra of each of its constituents. An *in situ* study of lobster shell by McKenthum [119] demonstrated a variety of pigment-protein species. Recording PA spectra at different modulation frequencies and using phase information, these workers found an anisotropic distribution of pigment in the shell attributable to protein-protein, pigment-protein and pigment-pigment interaction. This anisotropy disappeared after denaturation.

Photoacoustic depth profiling of double-layer biological samples using the two-signal phase-resolved method was done by many workers [122, 123, 127]. In this analysis, the signal from the surface and internal layers were separated using the phase-angle resolution method (from the in-phase and quadrature signal) to obtain the magnitude and phase spectra. Such a monitoring of the in-phase and quadrature signals is now a standard practice. Anjo and Moore [122] used the method to study the depth profile of β -carotene in skin. The spectrum of an induced layer of β -carotene in albino mouse skin was separated from the spectrum of hemoglobin. Dyes were then used to determine more precisely the position of the β -carotene in the epidermis.

Recently, Neri et al. [127] used the two-signal phase-resolved method for monitoring temporal changes occurring in a soybean leaf under the action of a herbicide. Using the PRM method described in section 3 Neri et al. [127] were able to monitor the phase shift between the cuticle and pigment layers as a function of the time elapsed after herbicide (Paraquat) spraying. This is shown in fig. 42. The authors suggested that the action of the herbicide on the soybean leaf is to cause a shrinkage of the leaf due to the induced dehydration as reflected in the decrease of the phase shift of the PA signal. This hypothesis was further checked by *in-vivo* monitoring of the thickness of the soybean leaf under the action of Paraquat. The measurements were done using an optical microscope with the leaf being kept between two glass plates and artificially illuminated with a 160 W tungsten filament lamp. The results

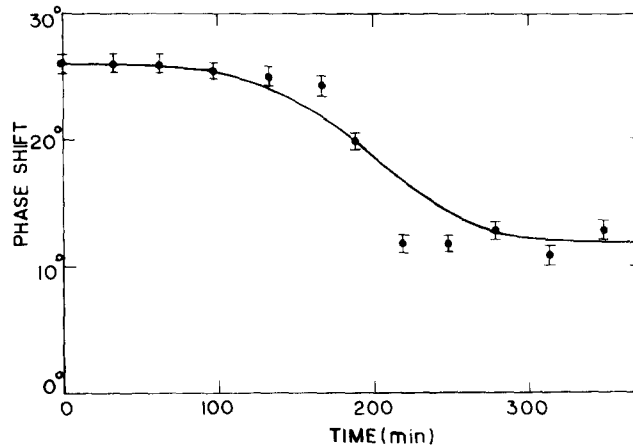


Fig. 42. Phase shift between the cuticle and the pigment layers in *Glycine max* (soybean) as a function of time (after Neri et al. [127]).

for the change of the leaf thickness as a function of the time elapsed after the spraying of Paraquat are shown in fig. 43.

Various examples of the use of PAS on intact green leaf have been reported. For example, Lima et al. [275] demonstrated that PAS is an efficient tool for the non-destructive assessment of chlorophyll and carotenoid deficient mutants of *Zea mays* L. The results were compared with those obtained applying some commonly used destructive techniques. In another work Lima et al. [276] presented evidence that PAS can be a very useful complementary tool in assessing plant productivity at some stage of its development. In addition to the usual spectroscopic information such as band positions and relative intensities, photoacoustic spectroscopy can offer new information that arises uniquely from the combination of spectroscopic and calorimetric phenomena that comprise the PA effect. This information includes quantum yields, lifetimes from various metastable excited states, and the kinetics of

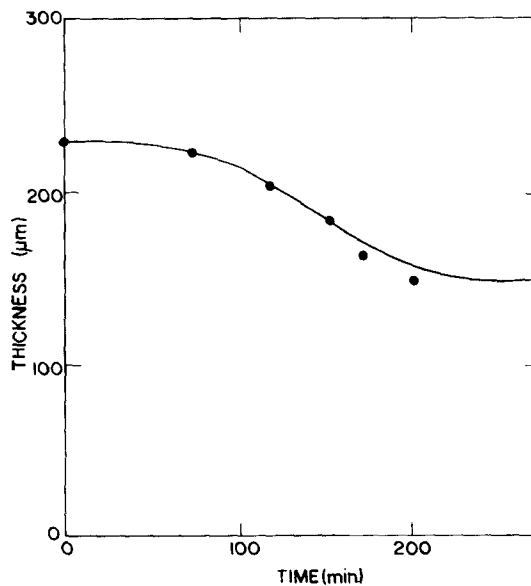


Fig. 43. Change of leaf thickness of *Glycine max* (soybean) as a function of the time elapsed after the spraying of Paraquat (after Neri et al. [127]).

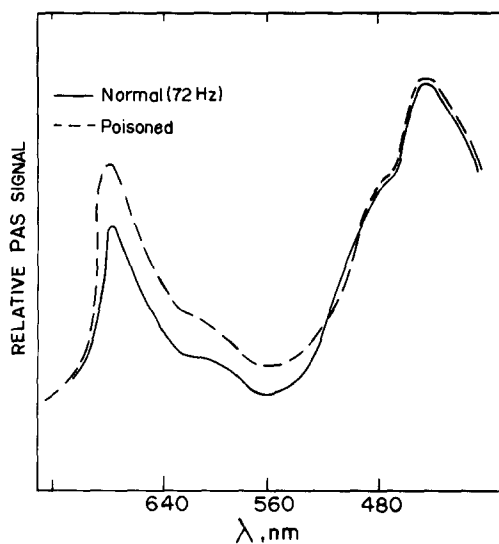


Fig. 44. Photoacoustic spectra of photosynthetically active (solid line) and photosynthetically inactive (dashed line) lettuce chloroplasts. The photosynthetically inactive sample was immersed in a DCMU saturated methanol bath and allowed to dry. DCMU is 3-(3,4-dichlorophenyl)-1-dimethylurea, an electron transport inhibitor. (After Cahen [278])

relaxation pathways of photobiological systems [271, 277]. The frequency dependence of the PA signal can give information on the amounts of energy stored in intermediates of biological photoprocesses [278–283]. Cahen et al. [278] studied photosynthesis in lettuce chloroplasts. Figure 44 shows the PAS spectra obtained for photosynthetically active membranes and for DCMU poisoned ones. The spectra are normalized at 440 nm where little photosynthetic activity is to be expected. At the 680 nm chlorophyll band, the DCMU poisoned chloroplasts give a signal that is 10% stronger than that of the active chloroplasts. As the modulation frequency is decreased, the difference between the spectra of normal and poisoned membranes increases.

Carpentier et al. [281, 282] reported on the use of PAS to study photosynthesis in algae and in leaves. Recently the same group [283] used the technique to monitor photosynthetic energy storage in heterosystems. Three main energy conversion pathways have been identified in these cells.

In the area of dermatology, PAS has been used particularly for studying the effects of active drugs in the skin. This was first demonstrated by Campbell et al. [284] by carrying out drug detection and determination of the drug diffusion rate in the human skin. These authors have also determined the thermal properties and water content of the skin. From the decay of the PA signal the diffusion coefficient of TCN (tetracycline) was found to be about 25 times smaller than that of water in palmar skin. Using an open-ended cell Giese et al. [285] reported in-vivo measurements on human skin treated with sunscreens. Poulet and Chambron [286] described an open-ended cell for in-vivo PA spectroscopy of the skin. As demonstrated by the authors a satisfactory signal-to-noise ratio can be obtained by using a differential microphone. Finally, in the area of foodstuff quality control some applications of PAS on the monitoring of foodstuff adulterants have also appeared in the literature [287, 288].

To date, the gas-microphone technique has probably been the most widely used technique for biological applications. However, photothermal radiometry, mirage effect and PZT detection are important variations that can provide key information on certain specific applications.

10. Concluding remarks

The field of photothermal science has partially fulfilled some of its promises since its rediscovery almost fifteen years ago by Rosencwaig. Yet its potential as a research and analytical tool seems to be not fully explored and each year new routes for developments are being opened up. Some of these developments are moving closer to industrial applications as testing and quality control techniques. Already, some of these photothermal techniques have been tested in the microelectronics and foodstuff industries. In the coming years, however, the number of these industrial applications should rapidly increase. Its ease of operation and versatility together with the wealth of information contained in the photothermal signal warrants us that further areas of applied research will adapt these techniques to their own uses. Furthermore, since these techniques are not both detector and pumping beam limited, they will surely be extended into ultrasonics and high-energy regions of the spectrum. In fact, some photothermal detections of X-ray and synchrotron radiation are appearing in the literature, and based upon the previous experience, the number of applications of these techniques in this high-energy region is bound to increase considerably, especially in the fields of biology and medicine.

In this work we have reviewed some experiments with the photothermal effect in the fields of physics, chemistry, biology, and medicine. In all these fields we have done no more than give a bird's eye view and indicate a limited number of applications of these techniques as dictated by our own interest and experience. Many other applications have been omitted and further references can be found in the previous review articles cited.

Acknowledgments

We are grateful to the many collaborators and students we had the pleasure to interact with and learn from over the years. Special thanks are due to our colleague, Dr. C.C. Ghizoni, for the sharpness of his arguments brought into our many discussions and who together with us pioneered the field of photoacoustics in the southern hemisphere. The long-standing collaboration with Professor J. Pelzl and his group from Bochum University, partly supported by the Internationale Büro der KFA Jülich, is gratefully acknowledged. This work was supported in part by the Brazilian agencies CNPq, FAPESP and FINEP. Finally, we are very grateful to our home institutions for the continuing support to our research groups.

References

- [1] L.B. Kreuzer, *J. Appl. Phys.* 42 (1971) 2934.
- [2] A. Rosencwaig, *Opt. Commun.* 7 (1973) 305.
- [3] A. Rosencwaig, *Science* 181 (1973) 657.
- [4] A. Rosencwaig, *Phys. Today* 28 (1975) no. 9, 23.
- [5] A. Rosencwaig, *Adv. Electron. Electron Phys.* 46 (1978) 207.
- [6] C.K.N. Patel and A.C. Tam, *Rev. Mod. Phys.* 53 (1981) 517.
- [7] J.B. Kinney and R.H. Staley, *Annu. Rev. Mater. Sci.* 12 (1982) 295.
- [8] G.F. Kirkbright and S.L. Castleden, *Chem. Br.* 16 (1980) 661.
- [9] G.A. West, J.J. Barrett, D.R. Siebert and K.V. Reddy, *Rev. Sci. Instrum.* 54 (1983) 797.
- [10] K. Klein, J. Pelzl and H. Futterer, in: *Photoacoustics, Principles and Applications*, eds E. Lüscher, P. Korpiun, H.J. Coufal and R. Tilgner (Vieweg, Braunschweig, 1982).

- [11] Y.H. Pao, *Opto-acoustic Spectroscopy and Detection* (Academic Press, New York, 1977).
- [12] A. Rosencwaig, *Photoacoustics and Photoacoustic Spectroscopy* (Wiley, New York, 1980).
- [13] A. Mandelis, ed., *Photoacoustic and Thermal Wave Phenomena in Semiconductors* (North-Holland, Amsterdam, 1987).
- [14] A. Rosencwaig and A. Gersho, *Science* 190 (1975) 556.
- [15] A. Rosencwaig and A. Gersho, *J. Appl. Phys.* 47 (1976) 64.
- [16] J.G. Parker, *Appl. Opt.* 12 (1973) 2974.
- [17] M.J. Adams, G.F. Kirkbright and K.R. Menon, *Anal. Chem.* 51 (1979) 508.
- [18] A. Rosencwaig, *Rev. Sci. Instrum.* 48 (1977) 1133.
- [19] G.C. Wetsel Jr and F.A. McDonald, *Appl. Phys. Lett.* 30 (1977) 252.
- [20] J.F. McClelland and R.N. Kniseley, *Appl. Phys. Lett.* 28 (1976) 467.
- [21] C.L. Cesar, C.A.S. Lima, N.F. Leite, H. Vargas, A.F. Rubira and F. Galembeck, *J. Appl. Phys.* 57 (1985) 4431.
- [22] P. Poulet, J. Chambon and R. Unterreiner, *J. Appl. Phys.* 51 (1980) 1738.
- [23] Y.C. Teng and B.S.H. Royce, *J. Opt. Soc. Am.* 70 (1980) 557.
- [24] S. Malkin and D. Cahen, *Anal. Chem.* 53 (1981) 1426.
- [25] E.M. Monahan Jr and A.W. Nolle, *J. Appl. Phys.* 48 (1977) 3519.
- [26] A. Hordvik and H. Schlossberg, *Appl. Opt.* 16 (1977) 101.
- [27] L.C. Aamodt, J.C. Murphy and J.G. Parker, *J. Appl. Phys.* 48 (1977) 927.
- [28] M.A. Fromowitz, P.S. Yeh and S. Yee, *J. Appl. Phys.* 48 (1977) 209.
- [29] F.A. McDonald and G.C. Wetsel, *J. Appl. Phys.* 49 (1978) 1313.
- [30] F.A. McDonald, *Appl. Opt.* 18 (1979) 1363.
- [31] H.S. Bennett and R.A. Forman, *J. Appl. Phys.* 48 (1977) 1432.
- [32] C.L. Cesar, H. Vargas, J.A. Meyer and L.C.M. Miranda, *Phys. Rev. Lett.* 42 (1979) 1570.
- [33] R.S. Quimby and W.M. Yen, *J. Appl. Phys.* 51 (1980) 4985.
- [34] F.A. McDonald, *Can. J. Phys.* 64 (1986) 1023.
- [35] P. Korpiun and B. Büchner, *Appl. Phys. B* 30 (1983) 121.
- [36] P. Korpiun, B. Büchner, A.C. Tam and Y.H. Wong, *Appl. Phys. Lett.* 46 (1985) 1039.
- [37] P. Korpiun, B. Büchner, A.C. Tam and Y.H. Wong, *J. Appl. Phys.* 59 (1986) 2944.
- [38] L.C. Aamodt and J.C. Murphy, *Can. J. Phys.* 64 (1986) 1221.
- [39] C.L. Cesar, Ph.D. Thesis, Univ. of Campinas (1985), unpublished.
- [40] R.S. Quimby and W.M. Yen, *J. Appl. Phys.* 52 (1981) 500.
- [41] C.A.S. Lima, L.C.M. Miranda and R. Santos, *J. Appl. Phys.* 52 (1981) 137.
- [42] A. Rosencwaig, *J. Appl. Phys.* 52 (1981) 503.
- [43] J.L. Parpal, J.P. Monchalín, L. Bertrand and J.M. Gagné, *J. Appl. Phys.* 52 (1981) 6879.
- [44] G. Rousset, F. Lepoutre and L. Bertrand, *J. Appl. Phys.* 54 (1983) 2383.
- [45] N.F. Leite, N. Cella, H. Vargas and L.C.M. Miranda, *J. Appl. Phys.*, in press.
- [46] A. Torres-Filho, L.F. Perondi and L.C.M. Miranda, *J. Appl. Pol. Sci.*, in press.
- [47] L.F. Perondi and L.C.M. Miranda, *J. Appl. Phys.*, in press.
- [48] J.B. Callis, *J. Res. Natl. Bur. Stand. A80* (1976) 413.
- [49] A. Hordvik and L. Skolnik, *Appl. Opt.* 16 (1977) 2919.
- [50] W. Lahmann, J.J. Ludewig and H. Welling, *Chem. Phys. Lett.* 45 (1977) 177.
- [51] S. Oda, T. Sawada and K. Kamada, *Anal. Chem.* 50 (1978) 865.
- [52] M.M. Farrow, R.K. Burnham, M. Auzaneau, S.L. Olsen, N. Purdie and E.M. Eyring, *Appl. Opt.* 17 (1978) 1093.
- [53] P. Helander, *J. Photoacoust.* 1 (1982) 103.
- [54] P. Helander, *J. Photoacoust.* 1 (1982) 203.
- [55] P. Helander and I. Lundström, *J. Appl. Phys.* 54 (1983) 5069.
- [56] P. Helander, *J. Photoacoust.* 1 (1982) 252.
- [57] P. Helander, *J. Appl. Phys.* 59 (1986) 3339.
- [58] D.H. McQueen, *J. Phys. E* 16 (1983) 738.
- [59] M.D. da Silva, I.N. Bandeira and L.C.M. Miranda, *J. Phys. E*, in press.
- [60] G.C. Wetsel Jr, *J. Opt. Soc. Am.* 70 (1980) 471.
- [61] W. Jackson and N.M. Amer, *J. Appl. Phys.* 51 (1980) 3343.
- [62] A.C. Boccara, D. Fournier and J. Badoz, *Appl. Phys. Lett.* 36 (1980) 130.
- [63] A.C. Boccara, D. Fournier, W. Jackson and N.M. Amer, *Opt. Lett.* 5 (1980) 377.
- [64] D. Fournier, A.C. Boccara, N.M. Amer and R. Gerlach, *Appl. Phys. Lett.* 37 (1980) 519.
- [65] J.C. Murphy and L.C. Aamodt, *J. Appl. Phys.* 51 (1980) 4580.
- [66] W.D. Jackson, N.M. Amer, A.C. Boccara and D. Fournier, *Appl. Opt.* 20 (1980) 1331.
- [67] A. Mandelis, *J. Appl. Phys.* 54 (1983) 3404.
- [68] B.S.H. Royce, F. Sánchez-Sinencio, R. Goldstein, R. Muratore, R. Williams and W.M. Yim, *Bull. Am. Phys. Soc.* 27 (1982) 243.

- [69] S.O. Kanstad and P.E. Nordal, *Powder Technol.* 22 (1978) 133.
- [70] P.E. Nordal and S.O. Kanstad, *Phys. Scr.* 20 (1979) 659.
- [71] P.E. Nordal and S.O. Kanstad, *Appl. Phys. Lett.* 38 (1981) 486.
- [72] S.O. Kanstad and P.E. Nordal, *Appl. Surf. Sci.* 6 (1980) 372.
- [73] R. Santos and L.C.M. Miranda, *J. Appl. Phys.* 52 (1981) 4194.
- [74] R.D. Tom, E.P. O'Hara and D. Benin, *J. Appl. Phys.* 53 (1982) 5392.
- [75] A.C. Tam and B. Sullivan, *Appl. Phys. Lett.* 43 (1983) 333.
- [76] W.P. Leung and A.C. Tam, *Opt. Lett.* 9 (1984) 893.
- [77] A.C. Tam, *Infrared Phys.* 25 (1985) 305.
- [78] S.O. Kanstad and P.E. Nordal, *Can. J. Phys.* 64 (1986) 1155.
- [79] P.E. Nordal and S.O. Kanstad, in: *Scanned Image Microscopy*, ed. E. Ash (Academic Press, New York, 1980).
- [80] A. Lehto, J. Jaarinen, T. Tiisanen, M. Jokinen and M. Luukkala, *Electron. Lett.* 17 (1981) 364.
- [81] D.P. Almond, P.M. Patel and H. Reiter, *J. Physique Coll. C6*, 44 (1983) 491.
- [82] P. Cielo, *J. Appl. Phys.* 56 (1984) 230.
- [83] H. Ermert, F.H. Dacol, R.L. Melcher and T. Baumann, *Appl. Phys. Lett.* 44 (1984) 1136.
- [84] G. Busse, *Infrared Phys.* 20 (1980) 419.
- [85] G. Busse, in: *Scanned Image Microscopy*, ed. E. Ash (Academic Press, New York, 1980).
- [86] M. Luukkala, in: *Scanned Image Microscopy*, ed. E. Ash (Academic Press, New York, 1980).
- [87] G. Busse, *Appl. Opt.* 31 (1982) 107.
- [88] G. Busse and K.F. Renk, *Appl. Phys. Lett.* 42 (1983) 366.
- [89] G. Busse and P. Eyerer, *Appl. Phys. Lett.* 43 (1983) 355.
- [90] J. Stone, *Appl. Opt.* 12 (1973) 1828.
- [91] A. Hordvik, *Appl. Opt.* 16 (1977) 2827.
- [92] Y. Ohtsuka and K. Itoh, *Appl. Opt.* 18 (1979) 219.
- [93] S. Ameri, E.A. Ash, V. Neuman and C.R. Petts, *Electron. Lett.* 17 (1981) 337.
- [94] L.C.M. Miranda, *Appl. Opt.* 22 (1983) 2882.
- [95] M.A. Olmstead, N.M. Amer, S. Kohn, D. Fournier and A.C. Boccara, *Appl. Phys. A* 32 (1983) 141.
- [96] R.C.C. Leite, R.S. Moore and J.R. Whinnery, *Appl. Phys. Lett.* 5 (1964) 141.
- [97] J.R. Whinnery, *Acc. Chem. Res.* 7 (1974) 225.
- [98] R.L. Swofford and J.A. Morrell, *J. Appl. Phys.* 49 (1978) 3667.
- [99] S.J. Sheldon, L.V. Knight and J.M. Thorpe, *Appl. Opt.* 21 (1982) 1663.
- [100] L.C.M. Miranda, *Appl. Phys. A* 32 (1983) 87.
- [101] H. Coufal, *Appl. Phys. Lett.* 44 (1984) 59.
- [102] A. Mandelis, *Chem. Phys. Lett.* 108 (1984) 388.
- [103] A. Mandelis and M. Zver, *J. Appl. Phys.* 57 (1985) 4421.
- [104] C.C. Ghizoni and L.C.M. Miranda, *Phys. Rev. B* 32 (1985) 8392.
- [105] H. Coufal and P. Hefferle, *Appl. Phys. A* 38 (1985) 213.
- [106] H. Coufal, *J. Vac. Sci. Technol. A* 5 (1987) 2875.
- [107] S.B. Lang, *Sourcebook of Pyroelectricity* (Gordon and Breach, London, 1974).
- [108] P.K. John, L.C.M. Miranda and A.C. Rastogi, *Phys. Rev. B* 34 (1986) 4342.
- [109] H. Coufal and P. Hefferle, *Can. J. Phys.* 64 (1986) 1200.
- [110] A. Mandelis, F. Care, K.K. Chan and L.C.M. Miranda, *Appl. Phys. A* 38 (1985) 117.
- [111] I.F. Faria Jr, C.C. Ghizoni, L.C.M. Miranda and H. Vargas, *J. Appl. Phys.* 59 (1986) 3294.
- [112] I.F. Faria Jr, C.C. Ghizoni and L.C.M. Miranda, *Appl. Phys. Lett.* 47 (1985) 1154.
- [113] M.J. Adams and G.F. Kirkbright, *Analyst* 102 (1977) 678.
- [114] M.J. Adams and G.F. Kirkbright, *Spectrosc. Lett.* 9 (1976) 255.
- [115] D. Betteridge, T.C. Lilley and P.J. Meyler, *Frezenius Z. Anal. Chem.* 296 (1979) 28.
- [116] P. Helander and I. Lundström, *J. Appl. Phys.* 52 (1981) 1146.
- [117] M. Morita, *Jpn. J. Appl. Phys.* 20 (1981) 835.
- [118] S.D. Campbell, S.S. Yee and M.A. Afromowitz, *IEEE Trans. Biomed. Eng. BME* 26 (1979) 220.
- [119] M.L. McKenthum, R.D. Tom and T.A. Moore, *Nature* 279 (1979) 215.
- [120] M.V. Iravani and H.K. Wickramasinghe, *J. Appl. Phys.* 58 (1985) 122.
- [121] J. Baumann and R. Tilgner, *J. Appl. Phys.* 58 (1985) 1982.
- [122] D.M. Anjo and T.A. Moore, *Photochem. Photobiol.* 39 (1984) 635.
- [123] E.P. O'Hara, R.D. Tom and T.A. Moore, *Photochem. Photobiol.* 38 (1983) 709.
- [124] C.L. Cesar, H. Vargas, J. Pelzl and L.C.M. Miranda, *J. Appl. Phys.* 55 (1984) 3460.
- [125] C.L. Cesar, H. Vargas and L.C.M. Miranda, *J. Phys. D* 18 (1985) 599.
- [126] U. Netzelmann, J. Pelzl, H. Vargas, C.L. Cesar and L.C.M. Miranda, *IEEE Trans. Magn. M* 5 (1984) 1252.

- [127] J.W. Neri, O. Pessoa Jr, H. Vargas, F.A.M. Reis, A.C. Gabrielli, L.C.M. Miranda and C. Vinha, *Analyst*, in press.
- [128] G.A.R. Lima, MSc. Thesis, Univ. of Campinas (1986), unpublished.
- [129] A. Mandelis and B.S.H. Royce, *J. Opt. Soc. Am.* 70 (1980) 474.
- [130] Y.H. Wong, R.L. Thomas and G.F. Hawkins, *Appl. Phys. Lett.* 32 (1987) 538.
- [131] M. Luukkala and A. Penttinen, *Electron. Lett.* 15 (1979) 326.
- [132] G. Busse, *Appl. Phys. Lett.* 35 (1979) 759.
- [133] A. Rosencwaig, *Electron. Lett.* 16 (1980) 928.
- [134] R.L. Thomas, J.J. Pouch, Y.H. Wong, L.D. Favro, P.K. Kuo and A. Rosencwaig, *J. Appl. Phys.* 51 (1980) 1152.
- [135] P.K. Kuo, L.D. Favro, L.J. Inglehart, R.L. Thomas and M. Srinivasan, *J. Appl. Phys.* 53 (1982) 1258.
- [136] K.R. Grice, L.J. Inglehart, L.D. Favro, P.K. Kuo and R.L. Thomas, *J. Appl. Phys.* 54 (1983) 6245.
- [137] Shu-Yi Zhang and L.I. Chen, *Can. J. Phys.* 64 (1986) 1316.
- [138] R.A. MacFarlane and L.D. Hess, *Appl. Phys. Lett.* 36 (1981) 137.
- [139] E.A. Ash, ed., *Scanned Image Microscopy* (Academic Press, New York, 1980).
- [140] A. Rosencwaig and G. Busse, *Appl. Phys. Lett.* 36 (1980) 725.
- [141] A. Rosencwaig, *J. Appl. Phys.* 51 (1980) 2210.
- [142] G.S. Cargill, *Nature* (1980) 691.
- [143] E. Brandis and A. Rosencwaig, *Appl. Phys. Lett.* 37 (1980) 98.
- [144] A. Rosencwaig and R.L. White, *Appl. Phys. Lett.* 38 (1981) 165.
- [145] M. Kasai, T. Sawada and Y. Gohshi, *Jpn. J. Appl. Phys.* 24 (1985) 220.
- [146] G.C. Wetsel Jr and F.A. McDonald, *Appl. Phys. Lett.* 41 (1982) 926.
- [147] L.J. Inglehart, K.R. Grice, L.D. Favro, P.K. Kuo and R.L. Thomas, *Appl. Phys. Lett.* 43 (1983) 446.
- [148] Y. Martin, H.K. Wickramasinghe and E.A. Ash, in: *Proc. 1982 IEEE Ultrasonics Symposium*, ed. B.R. McAvoy (IEEE, New York, 1982) p. 563.
- [149] Y.H. Wong, R.L. Thomas and J.J. Pouch, *Appl. Phys. Lett.* 35 (1979) 368.
- [150] H. Coufal, U. Möller and S. Schneider, *Appl. Opt.* 21 (1982) 2339.
- [151] T. Bauman, F. Dacol and R.L. Melcher, *Appl. Phys. Lett.* 41 (1983) 71.
- [152] R.L. Thomas, L.D. Favro and P.K. Kuo, *Can. J. Phys.* 64 (1986) 1234.
- [153] G. Diebold and D.L. McFadden, *Appl. Phys. Lett.* 29 (1976) 447.
- [154] C. Evora, R. Landers and H. Vargas, *Appl. Phys. Lett.* 36 (1980) 864.
- [155] O.A. Cleves Nunes, A.A.M. Monteiro and K. Skeff Neto, *Appl. Phys. Lett.* 35 (1979) 656.
- [156] W. Wettling, W. Jantz and L. Engelhardt, *Appl. Phys. A* 26 (1981) 19.
- [157] M. Davies and M. Heath, *J. Magn. Magn. Mater.* 31 (1983) 661.
- [158] R. Melcher, *Appl. Phys. Lett.* 37 (1980) 895.
- [159] U. Netzelmann, E.V. Goldammer, J. Pelzl and H. Vargas, *Appl. Opt.* 21 (1982) 1.
- [160] A. Vasson and A.M. Vasson, *J. Phys. D* 14 (1981) L39.
- [161] H. Coufal, *Solid State Commun.* 39 (1981) 467.
- [162] H. Vargas, in: *Photoacoustic Effect: Principles and Applications*, eds E. Lüscher, P. Korpiun, H. Coufal and R. Tilgner (Vieweg, Braunschweig, 1982).
- [163] J. Schmidt and I. Solomon, *J. Appl. Phys.* 37 (1966) 3719.
- [164] W.S. Moore and T.M. Al-Sharbaty, *J. Phys. D* 6 (1973) 367.
- [165] C.L. Cesar, H. Vargas, U. Netzelmann and J. Pelzl, *J. Magn. Magn. Mater.* 54 (1986) 1185.
- [166] U. Netzelmann and J. Pelzl, *Appl. Phys. Lett.* 44 (1984) 854.
- [167] M. Davies and M. Heath, *J. Phys. D* 18 (1985) 1655.
- [168] R.C. DuVarney, A.K. Garrison and G. Busse, *Appl. Phys. Lett.* 38 (1981) 675.
- [169] R.L. Melcher and G.V. Arbach, *Appl. Phys. Lett.* 40 (1982) 910.
- [170] U. Netzelmann, U. Krebs and J. Pelzl, *Appl. Phys. Lett.* 44 (1984) 1161.
- [171] P.C. Main and J.P.J. McCann, *J. Phys. D* 17 (1984) 522.
- [172] M.J. Adams, B.C. Beadle and G.F. Kirkbright, *Anal. Chem.* 50 (1978) 1371.
- [173] S.L. Castleden, G.F. Kirkbright and K.R. Menon, *Analyst* 105 (1980) 1076.
- [174] Q. Jin, G.F. Kirkbright and D.E.M. Spillane, *Appl. Spectrosc.* 36 (1982) 120.
- [175] C.M. Ashworth, G.F. Kirkbright and D.E.M. Spillane, *Analyst* 108 (1983) 1481.
- [176] C.H. Lochmuller and D.R. Wilder, *Anal. Chim. Acta* 11 (1980) 101.
- [177] M. Natale and L.N. Lewis, *Appl. Spectrosc.* 36 (1982) 410.
- [178] U. Haas, *Can. J. Phys.* 64 (1986) 1063.
- [179] M. Ganzarolli, O. Pessoa Jr, H. Vargas and F. Galembeck, *Polym. Sci.*, in press.
- [180] D.A. Saucy, S.J. Simko and W. Linton, *Anal. Chem.* 57 (1985) 871.
- [181] M.G. Rockley, *Chem. Phys. Lett.* 68 (1979) 455.
- [182] D.W. Virdine, *Appl. Spectrosc.* 34 (1980) 314.

- [183] M.G. Rockley, *Chem. Phys. Lett.* 75 (1980) 370.
- [184] M.J.D. Low and G.A. Parodi, *Spectrosc. Lett.* 11 (1978) 581.
- [185] M.J.D. Low and G.A. Parodi, *J. Mol. Struct.* 61 (1980) 119.
- [186] M.J.D. Low and G.A. Parodi, *J. Photoacoust.* 1 (1982) 131.
- [187] J.B. Kinney and R.H. Staley, *Anal. Chem.* 55 (1983) 343.
- [188] J.F. McClelland, *Anal. Chem.* 55 (1983) 89A.
- [189] L.B. Lloyd, S.M. Riseman, R.K. Burnham, E.M. Eyring and M.M. Farrow, *Rev. Sci. Instrum.* 51 (1980) 1488.
- [190] M.M. Farrow, R.K. Burnham and E.M. Eyring, *Appl. Phys. Lett.* 33 (1978) 735.
- [191] B.S.H. Royce, Y.C. Teng and J. Enns, in: *IEEE Ultrasonics Symp. Proc. (IEEE, New York, 1980) Vol. 2, p. 652.*
- [192] G. Laufer, J.T. Huneke, B.S.H. Royce and Y.C. Teng, *Appl. Phys. Lett.* 37 (1980) 517.
- [193] P.R. Solomon and R.M. Carangelo, *Fuel* 61 (1982) 663.
- [194] J.B. Kinney, R.H. Staley, C.L. Reichel and M.S. Wrighton, *J. Am. Chem. Soc.* 103 (1981) 4273.
- [195] M.G. Rockley, D.M. Davies and H.H. Richardson, *Appl. Spectrosc.* 35 (1981) 185.
- [196] M. Choquet, G. Rousset and L. Bertrand, *Can. J. Phys.* 64 (1986) 1081.
- [197] R.A. Palmer and M.J. Smith, *Can. J. Phys.* 64 (1986) 1086.
- [198] M.J.D. Low, G.A. Parodi and M. Lacroix, *Chem. Biomed. Environ. Instrum.* 11 (1981) 265.
- [199] M.J.D. Low and C. Morterra, *Appl. Spectrosc.* 38 (1984) 807.
- [200] Y.S. Touloukian, R.W. Powell, C.Y. Ho and M.C. Nicolasu, in: *Thermal Diffusivity (IFI/Plenum, New York, 1973).*
- [201] G. Ziegler and D.P.H. Hasselman, *J. Mater. Sci.* 16 (1981) 495.
- [202] B. Merté, P. Korpiun, E. Lüscher and R. Tilgner, *J. Physique Coll. C6, 44 (1983) 463.*
- [203] A.C. Bento, H. Vargas, M.M.F. Aguiar and L.C.M. Miranda, *Phys. Chem. Glasses* 28 (1987) 127.
- [204] R. Kordecki, B.K. Bein and J. Pelzl, *Can. J. Phys.* 64 (1986) 1204.
- [205] M.J. Adams and G.F. Kirkbright, *Analyst* 102 (1977) 281.
- [206] P. Charpentier, F. Lepoutre and L. Bertrand, *J. Appl. Phys.* 53 (1982) 608.
- [207] C.L. Cesar, H. Vargas, J. Mendes Filho and L.C.M. Miranda, *Appl. Phys. Lett.* 43 (1983) 555.
- [208] Z. Yaza and N. Amer, in: *Topical Meeting on Photoacoustic Spectroscopy (Ames, IA, 1979), paper WA5-1, unpublished.*
- [209] R.T. Swimm, *Appl. Phys. Lett.* 42 (1983) 955.
- [210] A. Lachaine and P. Poulet, *Appl. Phys. Lett.* 45 (1984) 953.
- [211] A. Lachaine, *J. Appl. Phys.* 57 (1985) 5076.
- [212] O. Pessoa Jr, C.L. Cesar, N.A. Patel, H. Vargas, C.C. Ghizoni and L.C.M. Miranda, *J. Appl. Phys.* 59 (1986) 1316.
- [213] M.A.J. Angström, *Philos. Mag.* 25 (1863) 181.
- [214] H. Vargas and L.C.M. Miranda, in: *Photoacoustics and Thermal Wave Phenomena in Semiconductors*, ed. A. Mandelis (North-Holland, Amsterdam, 1987).
- [215] E.F. Stegmeir, *Thermal conductivity*, in: *International Developments in Heat Transfer (ASME, New York, 1961).*
- [216] D.J. McNeill, *J. Appl. Phys.* 33 (1962) 597.
- [217] D. Grzegorzczak and G. Feineman, *Handbook of Plastics in Electronics (Reston Publ., Reston, VA, 1974).*
- [218] P.K. Kuo, M.J. Lin, C.B. Reyes, L.D. Favro, R.L. Thomas, D.S. Kim, Shu-yi Zhang, L.G. Inglehart, D. Fournier, A.C. Boccara and N. Yacoubi, *Can. J. Phys.* 64 (1986) 1165.
- [219] P. Cielo, L.A. Utracki and M. Lamontagne, *Can. J. Phys.* 64 (1986) 1172.
- [220] J.T. Dodgson, A. Mandelis and C. Andreetta, *Can. J. Phys.* 64 (1986) 1074.
- [221] S.O. Ferreira, C. Ying An, I.N. Bandeira, L.C.M. Miranda and H. Vargas, submitted for publication.
- [222] R. Florian, J. Pelzl, M. Rosenberg, H. Vargas and R. Wernhardt, *Phys. Status Solidi (a)* 48 (1978) K35.
- [223] M.A.A. Siqueira, C.C. Ghizoni, J.I. Vargas, E.A. Menezes, H. Vargas and L.C.M. Miranda, *J. Appl. Phys.* 51 (1980) 1403.
- [224] J. Fernandez, J. Etxebarria, J.J. Tello and A.L. Echarri, *J. Phys. D* 16 (1983) 269.
- [225] C. Pichon, M. Le Liboux, D. Fournier and A.C. Boccara, *Appl. Phys. Lett.* 35 (1979) 435.
- [226] P. Korpiun, J. Baumann, E. Lüscher, E. Papamokos and R. Tilgner, *Phys. Status Solidi (a)* 58 (1980) K13.
- [227] W. Knoll, J. Baumann, P. Korpiun and V. Theilen, *Biochem. Biophys. Res. Commun.* 96 (1980) 968.
- [228] P. Korpiun and R. Tilgner, *J. Appl. Phys.* 51 (1980) 6115.
- [229] P. Korpiun and R. Tilgner, *Phys. Status Solidi (a)* 67 (1982) 202.
- [230] P. Korpiun, R. Tilgner and O. Schmidt, *J. Physique Coll. C6 44 (1983) 43.*
- [231] K. Junge, B. Bein and J. Pelzl, *J. Physique Coll. C6, 44 (1983) 55.*
- [232] K. Klein and J. Pelzl, *J. Physique Coll. C6, 44 (1983) 227.*
- [233] F. Boucher and R. Leblanc, *Biochem. Biophys. Res. Commun.* 100 (1981) 385.
- [234] P.S. Bechthold and M. Campagna, *Optics Commun.* 36 (1981) 373.
- [235] P.S. Bechthold, M. Campagna and T. Schober, *Solid State Commun.* 36 (1980) 225.
- [236] G. Louts, P. Billard and B. Mangeot, *Can. J. Phys.* 64 (1986) 1230.
- [237] P.S. Bechthold, *J. Photoacoust.* 1 (1982) 87.
- [238] A. Mandelis, F. Care, K.K. Chan and L.C.M. Miranda, *Appl. Phys. A* 38 (1985) 117.

- [239] A. Rosencwaig, *Anal. Chem.* 47 (1975) 592.
- [240] I.O. Starobogatov, *Opt. Spectrosc.* 42 (1977) 172.
- [241] M.J. Adams, J.G. Highfield and G.F. Kirkbright, *Anal. Chem.* 49 (1977) 1850.
- [242] J.C. Murphy and L.C. Aamodt, *J. Appl. Phys.* 48 (1977) 3502.
- [243] L.D. Merkle and R.C. Powell, *Chem. Phys. Lett.* 46 (1977) 303.
- [244] R.S. Quimby and W.M. Yen, *Opt. Lett.* 3 (1978) 181.
- [245] G.J. Diebold, *J. Phys. Chem.* 84 (1980) 2213.
- [246] R.C. Gray and A.J. Bard, *Anal. Chem.* 50 (1978) 1262.
- [247] D. Cahen, *Appl. Phys. Lett.* 33 (1978) 810.
- [248] P.E. Nordal and S.O. Kanstad, *Infrared Phys.* 25 (1985) 302.
- [249] H.L. Riette, L.C.M. Miranda and H. Vargas, *Appl. Phys. A*, in press.
- [250] D. Cahen and S.D. Halle, *Appl. Phys. Lett.* 46 (1985) 446.
- [251] S.M.N. Mello, C.C. Ghizoni, L.C.M. Miranda and H. Vargas, *J. Appl. Phys.* 61 (1987) 5176.
- [252] W. Thielemann and H. Neumann, *Phys. Status Solidi (a)* 61 (1980) K123.
- [253] W. Thielemann and B. Rhielaender, *Solid State Electron.* 28 (1985) 1111.
- [254] I.N. Bandeira, H. Closs and C.C. Ghizoni, *J. Photoacoust.* 1 (1982) 275.
- [255] N. Mikoshiba, H. Nakamura and K. Tsubouchi, in: *IEEE Ultrasonics Symp. Proc. (IEEE, New York, 1982) Vol. 2, p. 580.*
- [256] L.C.M. Miranda, *Appl. Opt.* 21 (1982) 2923.
- [257] V.A. Sablikov and V.B. Sandomirskii, *Phys. Status Solidi (b)* 120 (1983) 471.
- [258] V.A. Sablikov and V.B. Sandomirskii, *Sov. Phys. – Semicond.* 17 (1983) 50.
- [259] A.N. Vasilev and V.B. Sandomirskii, *Sov. Phys. – Semicond.* 18 (1984) 1095.
- [260] A.N. Vasilev and V.B. Sandomirskii, *Sov. Phys. – Semicond.* 18 (1984) 1221.
- [261] K. Wasa, K. Tsubouchi and N. Mikoshiba, *Jpn. J. Appl. Phys.* 19 (1980) L475.
- [262] K. Wasa, K. Tsubouchi and N. Mikoshiba, *Jpn. J. Appl. Phys.* 19 (1980) L653.
- [263] A. Skumanich, D. Fournier, A.C. Boccara and N. Amer, in: *4th Intern. Meeting on Photoacoustic, Thermal and Related Sciences (Montreal, Quebec, 1985), paper WD-2.1 unpublished.*
- [264] C.C. Ghizoni, M.A.A. Siqueira, H. Vargas and L.C.M. Miranda, *J. Appl. Phys.* 32 (1978) 554.
- [265] H.N. Spector, in: *Solid State Physics, Vol. 19, eds F. Seitz and D. Turnbull (Academic Press, New York, 1966) p. 291.*
- [266] E.M. Ephstein, *Sov. Phys. – Semicond.* 9 (1976) 1043.
- [267] N.A.S. Rodrigues, C.C. Ghizoni and L.C.M. Miranda, *J. Appl. Phys.* 60 (1986) 1528.
- [268] N.A.S. Rodrigues, C.C. Ghizoni and L.C.M. Miranda, *Solid State Commun.* 60 (1986) 323.
- [269] T.A. Moore, *Photochem. Photobiol. Rev.* 7 (1983) 187.
- [270] D. Balasubramanian, *Biosci. Rep.* 3 (1983) 981.
- [271] D. Cahen, G. Bults, H. Garty and S. Malkin, *J. Biochem. Biophys. Methods* 3 (1980) 293.
- [272] D. Balasubramanian and Ch.M. Rao, *Can. J. Phys.* 64 (1986) 1132.
- [273] A. Rosencwaig, *Annu. Rev. Biophys. Bioeng.* 9 (1980) 31.
- [274] D. Balasubramanian, Ch.M. Rao and P. Panijpan, *Science* 223 (1984) 828.
- [275] C.A.S. Lima, H. Vargas, C.L. Cesar, M.B.S. Lima, L.M. Prioli and W.J. da Silva, *Plant Science* 38 (1985) 47.
- [276] C.A.S. Lima, J.C.V. Mattos, L.C.M. Miranda, A.F.S. Penna, J.F.W. von Bülow and C.C. Ghizoni, *J. Photoacoust.* 1 (1982) 61.
- [277] S. Malkin and D. Cahen, *Photochem. Photobiol.* 29 (1979) 803.
- [278] D. Cahen, S. Malkin and E.I. Lerner, *FEBS Lett.* 91 (1978) 339.
- [279] D. Cahen, H. Garty and S.R. Caplan, *FEBS Lett.* 91 (1978) 131.
- [280] S. Malkin, N. Lasser-Rosser, G. Bults and D. Cahen, in: *Photosynthesis III. Structure and Molecular Organization of the Photosynthetic Apparatus, Ed. G. Akoyunoglou-Balaban (Inst. Science Services, Philadelphia, PA, 1981) pp. 1031.*
- [281] R. Carpentier, B. Larue and R.M. Leblanc, *Arch. Biochem. Biophys.* 222 (1983) 403.
- [282] R. Carpentier, B. Larue and R.M. Leblanc, *Arch. Biochem. Biophys.* 228 (1984) 534.
- [283] R. Carpentier, H.C.P. Matthijs, R.M. Leblanc and G. Hind, *Can. J. Phys.* 64 (1986) 1136.
- [284] S.D. Campbell, S.S. Sinclair and M.A. Afromowitz, *IEEE Trans. Biomed. Eng. BME* 26 (1979) 220.
- [285] K. Giese, A. Nicolaus, B. Sennhenn and K. Kölmel, *Can. J. Phys.* 64 (1986) 1139.
- [286] P. Poulet and J. Chambron, *J. Physique Coll. C6*, 44 (1983) 413.
- [287] C.L. Cesar, C.A.S. Lima, H. Vargas and L.C.M. Miranda, *J. Agric. Food Chem.* 32 (1984) 1355.
- [288] P.S. Benton and S.S. Tanner, *Analyst* 108 (1983) 591.